Chapter 3:
Aircraft Instrumentation and Calibration

Chapter Contents

3.1 Introduction

The main role of the aircraft in the 1995 OASIS experiment was to provide measurements of the mean and turbulent components of the flow within the atmospheric boundary layer along a 96 km transect. The most important data required from the aircraft measurements were the vertical fluxes of heat, water vapour, carbon dioxide and momentum at the Earth's surface.

The FIAMS research aircraft used during the 1995 OASIS experiment was the Grob 109B *VH-HNK*. The aircraft will be referred to by its callsign, *HNK*, throughout this thesis. *HNK* carried instruments to measure the three components of the ambient wind field, air temperature, water vapour and carbon dioxide concentration, incoming and outgoing solar and terrestrial radiation and the surface temperature. The meteorological measurements were supported by instruments that recorded the aircraft height above ground level and above sea level, the air speed and ground speed of the aircraft and the orientation of the aircraft with respect to the local wind and the Earth.

The measurement of meteorological quantities from an airborne platform places stringent requirements on the accuracy and time response of the instruments because the air and ground speeds of the aircraft are an order of magnitude greater than the wind speed. The difficulties associated with the speed of the aircraft are further compounded by the movement in three dimensions and the flow deformation caused by the presence of the aircraft. Measurements made from airborne platforms need to have high absolute accuracy and fast response in order to overcome these difficulties. A single instrument does not usually meet the requirements of accuracy and fast response. The common solution to this problem is to use two instruments to measure the same quantity, one with high accuracy but slow response and the second with fast response but lower accuracy. The two data streams are then merged to provide a single data series with the best features of both instruments (Leise and Masters, 1991).

The accuracy of any measurement can only be guaranteed by careful and thorough calibration of the instruments involved. This is particularly evident in the case of

airborne observations where measurements by several instruments are often required to derive one meteorological quantity. A good example of this is provided by the calculation of the ambient wind field. On *HNK*, this requires a total of 17 quantities measured by eight different instruments.

The calibration of airborne instruments, particularly those involved in measuring the wind field, falls into two broad categories. The first of these is called static calibration and is performed with the sensor or aircraft at rest. An example of this is the calibration of a resistive temperature sensor to equate the resistance of the sensor to temperature. The second is called dynamic calibration and is performed with the aircraft in-flight. Dynamic calibration involves the execution of carefully planned aircraft manoeuvres designed to provide the information necessary to evaluate each term in a calibration model. An example of this type of calibration is the estimation of the temperature sensor recovery factor, which can only be done when the sensor is moving with respect to the air.

A description of the aircraft, the instrumentation, the calibration work undertaken and the known problems with the aircraft instruments during the 1995 OASIS experiment is presented in this chapter. Section 3.2 describes the aircraft, lists the instrument suite carried on the aircraft for the 1995 OASIS experiment and discusses some important aspects of the data acquisition and processing. Full descriptions of the instruments are given in Section 3.3. The calibration of the aircraft instruments is divided into three sections. Section 3.4 discusses the static calibration procedures that are performed with the instrument at rest. Dynamic calibration procedures, using data collected during special manoeuvres in dedicated calibration flights, are described in Section 3.5. The further optimisation of the wind measurement calibration using data collected during the 1995 OASIS experiment is discussed in Section 3.6. Several problems with the aircraft instruments were identified during the data processing and these are described in Section 3.7 and correction techniques are presented where possible. The chapter concludes with a summary and general remarks in Section 3.8. Details of the calibration techniques, models used and results obtained are presented in Isaac and Hacker (2004) and only summaries of the relevant methods and results are given here.

3.2 Aircraft, Instrumentation and Data

3.2.1 Aircraft

HNK belongs to a class of aircraft called motorised gliders. These aircraft are designed to combine modest gliding performance, typical glide ratios of 1:20, with modest powered performance, typical climb rates of 400 ft min^{-1}. The dimensions and performance of the aircraft are given in Table 2.5.

Table 3.1 Dimensions and performance of the Grob G109B (from Hacker and Schwerdtfeger, 1988).

Length	8.10 m
Wingspan	17.40 m
Maximum take-off weight	870 kg
Payload	100 kg
Crew	2
Normal cruising speed	40 - 50 m s^{-1}
Speed range for measurements	25 - 45 m s^{-1}
Range	> 1000 km
Endurance	> 10 hrs
Ceiling	~5000 m
Climb rate	2 - 3 m s^{-1}

3.2.2 Instrumentation

The meteorological instruments carried on *HNK* during the 1995 OASIS experiment are listed in Table 3.2. Instruments used to measure aircraft parameters are listed in Table 3.3. A brief description of the sensors is given in Section 3.3.

Table 3.2 Meteorological instruments carried on *HNK* during OASIS.

Parameter	Sensor	Comments
Static pressure	5-hole probe	Rosemount 1201 transducer
Airspeed		
magnitude	5-hole probe	Rosemount 1221D *IAS* transducer
direction	5-hole probe	Rosemount 1221VL Δp transducers x 2
Temperature		
slow, air	Meteolabor TP-3S	0.5 mm Cu/Co thermocouple
fast, air	FIAMS PT100	25 μm, reverse flow housing
surface, IR	Heimann KT-15	8 - 14 μm
Water vapour		
slow	Meteolabor TP-3S	chilled mirror dew point sensor
fast	NOAA IRGA	open path infra-red gas analyser
fast	AIR Lyman-α	open path UV absorption
Carbon dioxide		
slow	LICOR 6251	mounted in cabin, aspirated at 2 L min^{-1}
fast	NOAA IRGA	open path infra-red gas analyser
Radiation		
shortwave	Eppley PSP	incoming on canopy, outgoing under wing
longwave	Eppley PIR	incoming on canopy, outgoing under wing
spectral	FIAMS VEG-1	650 and 860 nm

Table 3.3 Aerological instruments carried on *HNK* during OASIS.

Parameter	Sensor	Comments
Position	Trimble TANS	aircraft position in Earth centred-Earth
	Vector GPS	fixed coordinates at 0.75 Hz
Velocity		
slow	Trimble TANS	aircraft velocity in Earth centred-Earth
	Vector GPS	fixed coordinates at 0.75 Hz
fast	Rockwell-Collins	aircraft acceleration in aircraft
	AHS-85	coordinates at 26 Hz
Attitude		
slow	Trimble TANS	aircraft pitch, roll and yaw in Earth
	Vector GPS	coordinates at 1.5 Hz
fast	Rockwell-Collins	aircraft pitch, roll and yaw in Earth
	AHS-85	coordinates at 26 Hz
Altitude		
pressure	5-hole probe	Rosemount 12421M transducer
radar	King KRA-10A	5 to 800 m range

3.2.3 Data Acquisition and Processing

All meteorological sensors, the pressure altitude and the radar altimeter have analogue outputs. The aircraft logger samples the analogue data at either 2 Hz (slow logging) or 20 Hz (fast logging). Slow logging is used for ferry flights, profiles and other operations where turbulence information is not required. Fast logging is used whenever high time resolution data are needed for calculating turbulent statistics. The analogue time step, either 0.5 seconds or 0.05 seconds depending on the logging mode, is used as the basic time step for all aircraft data processing. Data streams with different sampling rates are linearly interpolated onto the analogue time step during processing.

Aircraft acceleration, attitude and angular rates are available from the Attitude and Heading System (AHS-85, Rockwell-Collins, USA) at 2.6 Hz (slow logging) or 26 Hz (fast logging). The Global Positioning System (GPS) unit sends aircraft position and velocity data at an average rate of 0.75 Hz and attitude data (pitch, roll and heading) at an average rate of 1.5 Hz.

Basic data processing is performed using 'Routinen zur Auswertung Meteorologischer Forschungsflüge' (RAMF, Chambers et al., 1996), a general purpose time series analysis program written in FORTRAN, developed over many years at FIAMS by multiple authors and tailored to aircraft data. The first step in the data processing is the conversion of all meteorological quantities to SI units using sensor calibrations provided by the manufacturer or determined at FIAMS. This step includes calculation of the air temperature and water vapour concentration, correction of the measured static and total pressures for flow distortion effects and calculation of the true air speed and the angles of attack and sideslip.

The second step involves processing of the aircraft position, velocity and attitude data and interpolation of these quantities onto the analogue time step. Aircraft velocity is obtained directly from the GPS unit (low frequency) and by integrating the aircraft acceleration recorded by the AHS-85 (high frequency). Velocities derived from integrated accelerations are subject to low-frequency drift due to offsets in the accelerometer outputs and need to be corrected with stable, low-frequency velocity data. This comes from the GPS unit (Trimble, USA) for the horizontal

velocity components and from the pressure altitude (dp_a/dt) for the vertical velocity component. The fast (AHS-85) and slow (GPS and dp_a/dt) data streams are merged using the filtered difference technique described in Leise and Masters (1991). The main advantage of this approach over the traditional complementary filter technique is that differences between instruments usually vary more slowly than the quantities being measured. This makes the technique more robust during aircraft manoeuvres and when dropouts occur in the GPS data stream. A similar technique is used to combine the aircraft attitude data from the AHS-85 and the TANS Vector (Trimble, USA) GPS. Attitude rates of change are taken directly from the AHS-85 data and position directly from the GPS data.

Calculation of the ambient wind is done in the third step and includes correction for winds induced at the 5-hole probe tip as a result of changes in the aircraft attitude. Radiation quantities are calculated and incoming shortwave radiation corrected for the aircraft attitude in the fourth step and CO_2 concentration is calculated in the fifth. Further details of the processing, in particular the techniques used to calculate the turbulence statistics and spectral and cospectral power densities, are given in the relevant chapters of this thesis and in Isaac and Hacker (2004).

3.3 Description of Instrumentation

3.3.1 Data Logger

The data logger carried by *HNK* consists of an IBM-compatible Personal Computer (PC), which controls data acquisition, real time display and storage and an interface section that links the aircraft sensors to the PC. The interface section carries four analogue to digital converters, each of which provides 16 single ended analogue inputs, and several custom-built cards to provide timing signals and to receive data from the AHS-85 and the GPS. The data logger was designed and built at FIAMS (G. Wilkins, pers. comm.).

Analogue data is filtered using 4-pole Butterworth low-pass filters with a cutoff frequency of 40 Hz before being sampled at 20 Hz. The filter cutoff frequency, chosen at the time the logger was built, is higher than the value of 10 Hz recommended by Kaimal and Finnigan (1994) for a sampling frequency of 20 Hz. As a result, aliasing of power from signal frequencies between 10 and 40 Hz will occur but this is not expected to lead to significant contamination of the vertical fluxes for two reasons. First, the finite time constants of the sensors will limit the power in the signals at high frequencies. Second, at an airspeed of 40 m s^{-1}, the Nyquist frequency (10 Hz in this case) lies well into the inertial subrange where there is little transport of heat, moisture or momentum (Kaimal and Finnigan, 1994). Examination of scalar power spectra and cospectra with vertical velocity do not show any evidence of high frequency aliasing.

3.3.2 5-hole Probe and Pressure Sensors

The motion of the aircraft with respect to the air is measured using a 5-hole probe mounted at the front of the instrument pod suspended beneath the left wing. The tip of the 5-hole probe sits approximately 0.5 m in front of, and 0.3 m below, the leading edge of the wing and is 3.6 m left of the aircraft roll axis. Lenschow (1986) provides a general description of the 5-hole probe technique. Leise and Masters (1991) use a model of the flow over a sphere to derive exact relationships between pressure differences measured on the surface of the sphere and the incidence angles.

The probe consists of five holes drilled in the hemispherical end of a 35 mm diameter shaft, one at the centre of the hemisphere and four in two orthogonal pairs with each hole at 45° to the central port. The orthogonal pairs are aligned parallel to the vertical and lateral axes of the aircraft, to measure the angles of attack and sideslip respectively. Differential pressure sensors (1221VL, Rosemount Inc., USA) are used to measure the pressure differences across each pair of holes.

The central port is used to measure the total, static plus dynamic, pressure. Dynamic pressure is measured with a differential pressure sensor (1221D, Rosemount Inc., USA) connected between the central port and a ring of static pressure ports drilled radially into the probe shaft, approximately 75 mm behind the probe tip. Static pressure (1201, Rosemount Inc., USA) is measured at a manifold connecting the ring of static ports.

3.3.3 Air Temperature Sensors

The primary temperature sensor on *HNK* is a modified combined air and dew point temperature system (TP-3S, Meteolabor AG, Switzerland). This sensor uses a 0.5 mm copper-constantan thermocouple mounted in a cylindrical radiation shield attached to the 5-hole probe shaft to measure the air temperature. The electronics used to process the thermocouple voltage, and provide the cold junction temperature, are located inside the instrument pod beneath the left wing. The large diameter of the thermocouple wire makes the Meteolabor unsuitable for turbulence measurements in the boundary layer (Moore, 1986).

Fast response measurements of air temperature are made using a 25 μm diameter platinum wire element wound over a triangular former made from thin (<0.5 mm) fibreglass sheet with a nominal resistance of 100 Ω at 0 °C (PT100). The distance between the points of the triangular former is 15 mm, which gives a wire segment length to diameter ratio of $15/0.025 \approx 600$. This is larger than the value of 145 quoted by Friehe and Khelif (1992) for the Rosemount 102 temperature sensor but somewhat less than the value of ~1000 they suggest as necessary to achieve a fast enough response for the measurement of sensible heat flux. The PT100 element is mounted inside a reverse-flow housing that allows air to circulate over the element in

the reverse direction to the sensors motion. Reversing the direction of airflow over the element protects the fine wire from damage due to insects, particles and hydrometeors. The housing consists of a cylindrical body that is tapered at the front, open at the rear and has three radial exhaust tubes extending from the body near the front. Areas of low pressure form in the lee of the exhaust tubes and this causes air to be drawn out of the housing along the tubes. The instrument is mounted on the pod beneath the left wing and the associated bridge electronics are housed within the pod. The PT100 elements and the reverse flow housing were fabricated at FIAMS (G. Evans, pers. comm.).

3.3.4 Water Vapour and Carbon Dioxide Sensors

The primary water vapour instrument on *HNK* is a modified chilled mirror dew point hygrometer (TP-3S, Meteolabor AG, Switzerland) mounted at the rear of the instrument pod. This unit uses Peltier coolers to chill a small mirror until dew forms on the mirror surface, this is detected optically and the mirror temperature measured using a copper-constantan thermocouple.

The response time of the dew point sensor is of the order of one second, too slow for measuring the vertical flux of water vapour (Moore, 1986). During the OASIS experiments, fast response measurements of water vapour and carbon dioxide concentration were made using an open path infrared gas analyser (NOAA IRGA; Auble and Meyers, 1992) mounted on the leading edge of the left wing, adjacent to the instrument pod. The NOAA IRGA measures the concentration of H_2O and CO_2 by measuring the absorption of infrared radiation at three wavelengths (2.61, 3.96 and 4.22 μm for H_2O, reference and CO_2 respectively). Changes in the intensity of light at the reference wavelength are used to correct for variations in background light, changes in the transmissivity of the air in the optical path and degradation of the optical path due to the accumulation of dirt on the optical components. The response time of the instrument is about 0.07 s. Problems with the NOAA IRGA measurement of CO_2 concentration are discussed in Section 3.7.4.

Repeated calibrations of the NOAA IRGA in the lead up to the 1995 OASIS experiment showed that the CO_2 calibration frequently exhibited unexplained changes in offset of the order of 10 mg m^{-3}. A LICOR 6251 (LICOR Inc., Nebraska,

USA) was fitted inside the cabin of *HNK* to provide accurate measurements of the absolute CO_2 concentration. The LICOR 6251 is a closed path, non-dispersive, infrared gas analyser consisting of two optical cells, one for the gas sample being analysed and the other for a reference gas. The instrument alternately measures the absorption of infrared radiation (4.26 μm) in both the sample and reference cells and outputs a voltage proportional to the difference in these. During OASIS, the LICOR 6251 was operated in absolute mode where air is continuously pumped around a closed loop containing a chemical scrubber to remove CO_2 from the reference cell. The analyser was connected to an air intake in the cabin roof by a 1.5 m length of 6 mm outside diameter Teflon tubing and was aspirated at approximately 2 L min^{-1} by drawing air through the sample cell. A 1 μm Gelman filter was fitted to the inlet of the sample cell to prevent contamination of the optics.

3.3.5 Radiation Sensors

Four broad band and two narrow band radiation sensors were mounted on *HNK* during the 1995 OASIS experiment.

Incoming and outgoing shortwave radiation (0.4 to 3.0 μm) were measured using Eppley Precision Spectral Pyranometers (PSP, Eppley Labs, USA) mounted on the cabin roof and beneath the right wing. Incoming and outgoing longwave (5 to 50 μm) radiation were measured using Eppley Precision Infrared Radiometers (PIR) mounted beside the pyranometers. Net radiation was calculated from the separate components measured by the four radiometers.

Surface temperature was measured using a downward looking KT-15 infrared thermometer (Heimann AG, Germany) mounted in the instrument pod beneath the left wing. This instrument has a 4° viewing angle and measures irradiance in the band 8 to 14 μm. Reflected radiation at 650 and 860 nm was measured using a narrow band spectral radiometer built at FIAMS. The instrument has a 1° viewing angle and was mounted beneath the right wing.

3.3.6 Aircraft Motion Sensors

The aircraft acceleration in three axes, attitude angles (pitch, roll and heading) and the rate of change of the attitude angles were measured by the AHS-85. This unit differs from conventional inertial navigation systems (INS) in that it uses rotating piezoelectric sensors, rather than gimballed, orthogonal gyroscopes, to measure the aircraft acceleration and the pitch and roll rates. The AHS-85 integrates the measured angular rates internally and outputs both the rates and the angles themselves. A flux gate compass mounted on the aircraft tailplane measured the aircraft heading. Aircraft velocity is obtained by integrating the accelerations in the aircraft frame of reference and rotating the components to the Earth frame of reference using the measured attitude angles.

A GPS attitude system (TANS Vector, Trimble, USA) was installed on *HNK* and provided data on the position, velocity and attitude angles of the aircraft. This system measures the aircraft attitude angles by analysing phase differences between the GPS carrier signal received at a pair of antennae mounted on the fuselage (pitch axis) and another pair mounted on the wings (roll axis). Velocity information is obtained from the Doppler shift in the carrier signal and position from the timing of signals from several different satellites.

3.4 Static Calibrations: Methods and Results

3.4.1 General Remarks

Most instrument calibrations degrade with time and regular renewal of calibration is required to ensure the integrity of the measurements. This is particularly so in the case of airborne instruments where two sensors are often required to fulfil the conflicting needs of high absolute accuracy and fast response. The traditional approach of transferring calibration from a slow response but accurate sensor to a fast response sensor has several drawbacks, not least because of their differing response times, and should be avoided where possible.

Static calibrations are performed with the instrument at rest and provide the relationship between the sensor output and the physical quantity being measured. The effects of airflow, such as dynamic heating and flow distortion, on the instrument calibrations are considered in Section 3.5. Three static calibration techniques have been employed in the work described here; bench, in-situ and environmental chamber. Bench calibrations involve removing the instrument from the aircraft and using a laboratory calibration rig to varying the sensor environment while measuring the sensor output. An example of this type is the calibration of resistive temperature sensors by immersion in a liquid bath. In-situ calibration involves varying the sensor environment while it is still mounted on the aircraft. An example of this technique is passing an air stream of known water vapour concentration through a dew point hygrometer while it is installed on the aircraft. This technique then includes any effects of the sensor installation. The third technique is the use of an environmental chamber where the sensor is placed in an enclosed space and cycled through a range of temperatures and water vapour concentrations. This method allows both temperature and humidity to be varied at the same time and can be automated.

3.4.2 Data Logger

DC calibration of the data logger was done using a programmable voltage source to apply known voltages to the filter inputs. Voltage levels were checked using a

precision voltmeter and the digital counts from the data logger were recorded at each setting. The gain and offset for each filter/analogue-to-digital channel was then obtained by linear regression of the digital counts against the input voltage. A total of five such calibrations was performed from 1995 to 1998.

The gain values of the filter/analogue-to-digital channels showed a high degree of consistency with typical variations of less than 0.02% between calibrations. This is not significant compared to other uncertainties in the instrument calibrations. The offset values showed significant variation between calibrations of up to ±20 mV and these were traced to ground loops in individual instruments and changes in the aircraft wiring during a major overhaul in 1997. Both of these meant that the offsets applicable to the data collected during the 1995 OASIS experiment could not be determined because the exact configuration of the instruments and data logger could not be reproduced. Examples of the effect of a ±20 mV uncertainty on the most sensitive meteorological quantities are shown in Table 3.4.

Table 3.4 Uncertainties in air temperature from the Meteolabor (T_{aML}) and PT100 (T_{aRF}), absolute humidity from the Meteolabor (a_{ML}) and NOAA IRGA (a_{IR}), true airspeed (τ) and the angles of attack (α) and sideslip (β) due to an uncertainty of 20 mV in the data logger calibration (see text for details).

T_{aML} °C	T_{aRF} °C	a_{ML} gm^{-3}	a_{IR} gm^{-3}	τ ms^{-1}	α deg.	β deg.
~0.9	0.3	0.5	0.1	0.2	0.1	0.1

The uncertainties in T_{aRF}, a_{IR}, α and β are similar to or less than the uncertainties in the calibration of these quantities, see Sections 3.4.3, 3.4.4 and 3.4.5. Uncertainties in the data logger calibration are potentially significant for the true airspeed and for temperature and absolute humidity calculated from the Meteolabor instrument. The lack of certainty in the offset for individual channels means that it is not possible to apply corrections, the uncertainties in Table 3.4 represent a contribution to the overall errors in the aircraft observations from these instruments.

3.4.3 5-hole Probe and Pressure Sensors

The 5-hole probe requires no static calibration but dynamic calibration of the probe and, by implication, the associated pressure sensors, is the most important step to ensuring accurate determination of the wind vector from airborne measurements. The dynamic calibration of the 5-hole probe is discussed in Section 3.5.

The static calibration of pressure transducers requires access to a traceable, secondary standard pressure sensor and is best left to the original manufacturer. Rosemount, Inc recommends that their pressure transducers be returned to the factory for re-calibration every 12 months. This has not been done for *HNK* and is a serious outstanding calibration issue. The effects of continued use of the manufacturer calibration is reduced by the dynamic calibration procedures described in Section 3.5.

3.4.4 Temperature Sensors

3.4.4.1 Reverse Flow PT100

The measurement of temperature using a PT100 sensor relies on detecting small changes in the resistance of the sensor. At 25 °C, a change of 1 °C produces a change of only 0.34 Ω in the resistance of the PT100 element. The low sensitivity of resistance to temperature means that the standard polynomial for a PT100 sensor can not be used if the PT100 element is not exactly 100 Ω at 0 °C. This is the case for the FIAMS PT100 elements, where the typical variation in element resistance at 0 °C is of the order of 1 Ω. This means that the calibration curve relating resistance to temperature must be individually determined for each PT100 element.

Resistance versus temperature calibrations for ten PT100 elements were derived by immersing the elements in a bath of high purity (>99.8%) ethanol. Ethanol was chosen because it was readily available and has a low electrical conductivity. The temperature of the ethanol bath was varied by changing the temperature of the water jacket from 30 °C to 0 °C by the adding either hot water or ice. The temperature of both the ethanol bath and the water jacket was measured using a quartz thermometer (HP2801, Hewlett-Packard, USA). Measurements of the PT100 resistance were

made at different ethanol bath temperatures but only when the temperature difference between the ethanol bath and the surrounding water jacket was less than 0.5 °C. The PT100 resistance was measured using a four-wire bridge configuration and a precision digital multimeter (DMM, Yokogawa, Japan).

Uncertainties in the calibration method have not been quantified but the residuals between the raw data and the fitted lines never exceed 0.15 °C and the lack of scatter in the results indicates that the random errors are small. The largest source of error is likely to be parasitic resistances in the leads and their connection to the PT100 element under calibration. These are expected to be less than 0.1 Ω, giving an uncertainty in the absolute calibration of the PT100 element of less than 0.3 °C.

The stability of the individual PT100 sensor calibrations depends on the degree of contamination of the wire surface and changes in the wire tension. Evidence from five years of sensor operation and calibrations suggests that there is negligible drift in the calibration of the PT100 element in the reverse flow housing. This stability, coupled with the ease of calibration using the procedures described above and the high signal-to-noise ratio of immersion resistance sensors compared to thermocouple measurement lead to the adoption of the reverse flow PT100 measurement as the primary air temperature for the OASIS experiments. This was a change in established FIAMS procedure, which considered the Meteolabor thermocouple as the standard temperature.

3.4.4.2 Meteolabor Thermocouple

The second temperature sensor used on *HNK* during the OASIS experiments was the Meteolabor copper/constantan thermocouple. Thermocouple response to temperature is described by a polynomial whose coefficients depend on the type of the thermocouple junction. One of their attractions is their long-term stability. However, all thermocouple measurements rely on knowing the temperature of the "cold junction", where the thermocouple wires make contact with the conductors, usually copper, that connect the thermocouple to the subsequent electronics. In the case of the Meteolabor sensor, this temperature is called the reference temperature and is measured by a thermistor mounted on a printed circuit board inside the sensor

electronics. Historically, the calibration of this thermistor has been altered to force agreement between different temperature sensors on the aircraft.

The thermocouple sensor is mounted in the instrument pod carried beneath the left wing of *HNK*. The Meteolabor thermocouple and associated electronics were removed from the instrument pod and placed in an environmental chamber (AMDEL, Adelaide, South Australia) prior to the 1995 OASIS experiment. The temperature inside the chamber was varied from 40 °C to 10 °C over a period of several hours and air temperature inside the chamber measured by a quartz thermometer (HP2801, Hewlett-Packard, USA). Fans were placed inside the chamber, in addition to the chamber' s own circulation fan, to ensure that the air was well mixed and temperature gradients were minimised. Since both the air temperature thermocouple and the cold junction thermistor were inside the chamber, calibrations of both measurements were obtained at the same time.

These results show that the difference between the manufacturers calibration and that derived from the environmental chamber was less than 1% in slope and less than 0.2 °C in offset, both of which are within the uncertainty of the method. The results from the environmental chamber calibrations show that there is no basis for the practice of altering the reference temperature calibration to force agreement between different temperature sensors on *HNK*.

3.4.5 Water Vapour Sensors

3.4.5.1 Meteolabor Dew Point Hygrometer

Three calibrations of the Meteolabor dew point hygrometer were performed; one in the environmental chamber and two during the 1995 OASIS experiment when the instrument was mounted on the aircraft. The methods and results are summarised below.

The calibration of the Meteolabor dew point sensor in the environmental chamber was performed at the same time as the air temperature calibration. The Meteolabor was mounted in the middle of the chamber so that the chamber' s circulation fan ensured an adequate flow of air through the chilled mirror unit. The chamber was set to cycle through humidity values of 10, 30, 50, 70 and 90% at a temperature of

35 °C, corresponding to a range of dew point temperatures from -1 °C to 32 °C. A pump was used to draw off a small amount of air from the chamber and this was passed through a LICOR 6262 Infrared Gas Analyser (LICOR Inc, Nebraska, USA) to measure the water vapour concentration in the chamber. The LICOR 6262 was calibrated against a LICOR 610 Dew Point Generator (LICOR Inc, Nebraska, USA) before and after the calibration run. The results show that the difference between the manufacturer calibration and that derived from the LICOR 6262 during the environmental chamber run was less than 2% in slope with an offset of 0.7 °C. The error in the slope is within the estimated uncertainty of the method (5%) and the offset is close to the estimated uncertainty of 0.5 °C.

The second and third calibrations were performed in-situ during the 1995 OASIS experiment with the Meteolabor mounted in the instrument pod and with the sensor output recorded by the aircraft data logger. The LICOR 610 was used to pass air at seven dew points over the range 2.5 to 22.5 °C through the Meteolabor sensor and then to the LICOR 6262, which provided the reference values for the calibration. The results again showed that the error in the slope of the manufacturer calibration was less than 2% but offsets of 2.1 and 3.6 °C were observed. A 3 °C offset in dew point temperature is equivalent to an error in the specific humidity of about 3 g kg^{-1} at an air temperature of 20 °C. The origin of the offset is discussed in Section 3.7.3.

3.4.5.2 NOAA IRGA

FIAMS operates three NOAA IRGA instruments and has maintained another two instruments for the National Institute of Water and Atmospheric Research Inc., New Zealand, (NIWA). A total of 46 calibrations were performed on the five instruments during the period of work covered by this thesis, including 10 calibrations of the IRGA used on *HNK* during the OASIS95 experiment. The sensitivity of the instrument calibrations to temperature was also determined for each IRGA at three different H_2O and CO_2 concentrations. A bench calibration facility was established to enable the accurate calibration of the water vapour and carbon dioxide sensors used by FIAMS. Details specific to CO_2 are discussed in Section 3.4.6.

The LICOR 610 Dew Point Generator was used as the standard source of air with a known water vapour concentration. The calibration of this instrument was

guaranteed by routine maintenance at FIAMS in accordance with the manufacturer instructions and by return of the instrument to LICOR for overhaul at intervals of 12 to 24 months depending on usage. The NOAA IRGA calibration facility consists of an aluminium hood that fits over the IRGA optical path, the LICOR 610, the LICOR 6262, a set of calibration gas cylinders and a system of two-way valves with associated plumbing and flow controllers. Air from the LICOR 610 can be routed directly to the LICOR 6262 (6262 calibration mode) or via the NOAA IRGA calibration hood to the LICOR 6262 (IRGA calibration mode).

The inside of the aluminium hood was coated with Teflon, all plumbing was 6.25 mm diameter PTFE (Teflon) tubing to minimise equilibration times and tube lengths were kept as short as possible to minimise pressure differences. The equilibration time of the facility for H_2O was checked using a step change in the water vapour concentration of the air stream. Repeated tests showed that air leaving the complete system (lines plus IRGA hood) had reached 99% of the inlet H_2O concentration after 15 minutes when flushed at a flow rate of 2 L min^{-1}. The flow rate is reduced to 0.5 L min^{-1} for the calibration points to avoid errors due to pressure differences occurring across the system. Ports were set into the side of the NOAA IRGA calibration hood to allow a thermistor (44000, YSI Inc, Ohio, USA) to measure temperature and a pressure sensor (PA-3, AIR Inc, USA) to measure pressure inside the hood. This allows the mixing ratio of the exhaust air leaving the hood, which is measured by the LICOR 6262, to be converted to absolute humidity at conditions inside the hood. A quadratic equation is then fitted to the NOAA IRGA output voltage and the absolute humidity.

The NOAA IRGA sensitivity to absolute humidity is relatively stable over a 12-month period with a mean value of 5.2 ± 0.2 g m^{-3} V^{-1}. The calibration offset varies by approximately 2 g m^{-3} between the three calibrations performed during the 1995 OASIS experiment and by approximately 1.3 g m^{-3} in the 12 months between the calibrations on 28 October 1995 and 24 October 1996.

3.4.6 Carbon Dioxide Sensors

3.4.6.1 NOAA IRGA

CO_2 calibrations of the NOAA IRGA were performed at the same time as the H_2O calibrations and used the bench facility that was described in Section 3.4.5.2.

The calibration procedure for CO_2 was essentially the same as that used for H_2O. Calibration gas from special cylinders is passed through a manifold made from Teflon tubing and Teflon Swagelock fittings. Two-way valves allow the CO_2 calibration gas to be switched into the lines in place of the LICOR 610 air stream and directed to either the LICOR 6262 (6262 calibration mode) or via the NOAA IRGA calibration hood to the LICOR 6262 (IRGA calibration mode). The CO_2 mixing ratio of the exhaust gas from the IRGA hood is measured by the LICOR 6262 and converted to CO_2 partial density (units mg m^{-3}) using the temperature and pressure measured inside the hood. The CO_2 gas stream can also be directed to the inlet of the LICOR 610 in order to humidify the dry cylinder air when checking the cross-sensitivity of the NOAA IRGA CO_2 calibration to H_2O concentration.

A number of sources were used to provide CO_2 calibration gases. Ultra-high Purity (UHP) N_2 (999,999 ppm N_2, BOC Gases, Adelaide, South Australia) was used for zero-CO_2 gas as a cost-effective alternative to purchasing synthetic, CO_2-free air. The effect of using UHP N_2 as the zero gas was checked by comparing the LICOR 6262 zero and span settings with UHP N_2 in the reference cell with the settings when scrubbed air was passed through the reference cell. No difference was detected between the two sources of CO_2-free gas. Span gas comes from a β-standard CO_2-in-air (BOC Gases, Adelaide, South Australia) with a nominal CO_2 concentration of 398 ± 8 ppm. The 2% tolerance on the β-standard span gas was refined during the 1995 OASIS experiment by careful inter-comparison with precision assayed cylinders ($\pm$ <0.1 ppm, GASLAB, CSIRO, Australia) using the LICOR 6262. The mean of seven inter-comparisons performed on two separate days gave the CO_2 concentration of the β-standard as 399 ± 0.2 ppm. Cylinders of instrument-grade compressed air were then assayed against this β-standard to provide a source of working calibration gas.

The NOAA IRGA sensitivity to CO_2 partial density is relatively stable over a 12-month period with a mean value of 50 ± 2 mg m^{-3} V^{-1}. The typical noise level observed during the calibration runs was about ± 10 mV, which is equivalent to a noise level of ± 0.5 mg m^{-3} in the CO_2 concentration. The NOAA IRGA CO_2 calibration is stable enough for measurement of F_C but the noise level is similar to typical values of the standard deviation of CO_2 concentration ($\sigma_c = F_C / r_c \sigma_w \approx -0.3/(-0.3 \times 1) = 1$ mg m^{-3}). The implications of this are discussed in Section 3.7.4.

3.4.6.2 LICOR 6251

The LICOR 6251 CO_2 analyser is provided with a third order calibration polynomial by the manufacturer that relates the output voltage to the mixing ratio in the sample cell. The analyser fitted to *HNK* for the 1995 OASIS experiment was a new unit and the manufacturer calibration was current. The only adjustments required were periodic checks of the zero and span settings.

The zero and span settings for the LICOR 6251 were checked before and after the main flight on each day of aircraft operations during the 1995 OASIS experiment. The checks were performed with the LICOR 6251 mounted in the aircraft cabin and with the unit aspirated at the same rate as during data collection. None of the daily checks revealed a change of more than ± 2 ppm from day to day. The analyser zero and span controls were adjusted to give the correct readings when the zero and span readings differed by more than ± 1 ppm from the true values.

3.4.7 Radiation Sensors

3.4.7.1 Eppley Pyranometers

Eppley PSP 29711 was mounted beneath the right wing and measured the outgoing shortwave radiation. The manufacturer supplied a calibration for this instrument when it was purchased in June 1993 and this was used for the 1995 OASIS experiment. A subsequent calibration by the manufacturer in September 1996 gave values within 1% of the original.

Eppley PSP 29712 was mounted on the cabin roof and measured incoming shortwave radiation. The calibration used for this instrument was derived at FIAMS by comparison with a standard instrument (D. Pethick, pers. comm.) and expresses the coefficient as a weak function of solar zenith angle. The dependence is less than 5% for incidence angles less than 65°.

Katsaros and DeVault (1986) describe the correction of data from upward looking pyranometers for the effect of radiometer tilt. Saunders et al. (1991) and Bannehr and Schwiesow (1993) also discuss the measurement of radiation by airborne instruments including corrections for radiometer tilt. The full set of equations used to correct the data from *HNK* is presented in Isaac and Hacker (2004) along with a description of the assumptions and limitations of the method.

The pitch and roll offsets of the radiometer mountings and the phase difference between the radiometer output and the aircraft attitude angles must be specified before the tilt correction can be applied. Pitch and roll offsets were estimated from two direct measurements of the mounting orientation with respect to the AHS-85 and by minimising the variance in $S_{\downarrow}$ in data collected during reverse heading runs under clear skies. The averages of the three estimates are $-1.2 \pm 0.6°$ for the pitch offset and $0.1 \pm 0.1°$ for the roll offset. The uncertainty of $\pm 0.6°$ in the pitch offset produces a $\pm$ 2% variation in the incoming shortwave irradiance for a solar zenith of 60° with smaller errors at the smaller zenith angles typical of the 1995 OASIS data collection flights.

The phase difference between the radiometer and aircraft attitude data is due to the differing instrument response times, about 1 s and 0.04 s respectively. A recursive low-pass filter (Kaimal and Finnigan, 1994) was used to approximate the radiometer response and was applied to the aircraft attitude data before performing the correction for radiometer tilt due to aircraft pitch and roll motions. The filter performs two functions. First, it is non-symmetric and so it introduces a phase lag into the filtered attitude data that is proportional to the filter time constant. The time constant was chosen to minimise the phase difference between the radiometer data and the filtered attitude time series. Second, the filter attenuates high frequency

fluctuations in the attitude data, which, if not removed, would introduce high frequency noise into the corrected shortwave irradiance.

The phase delay between the radiometer output and the attitude data was estimated from the time lag at maximum correlation between pitch and $S_{\downarrow}$ using data collected during a series of pitching manoeuvres performed under a uniform cirrus layer. The delay was found to be 0.8 s and this was reduced to zero when a recursive low-pass filter was applied to the attitude data with a filter time constant of 1 s. This result agrees with the value of 1 s given by Saunders et al. (1991) for the time constant of the Eppley PSP instruments. Application of the radiometer tilt correction reduced the peak-to-peak variation in the shortwave irradiance recorded during the pitching manoeuvre from 500 W m^{-2} to less than 100 W m^{-2}. Aircraft pitch angles during this manoeuvre were ± 15°, much greater than those encountered during data collection runs.

3.4.7.2 Eppley Pyrgeometers and Heimann Infra-red Thermometer

Eppley PIR 29713 was mounted beneath the right wing to measure outgoing longwave radiation and Eppley PIR 29714 was mounted on the cabin roof to measure incoming longwave radiation. Both instruments used the internal thermal compensation method employed by Eppley, Inc. The manufacturer calibration was used for the Eppley PIR and Heimann KT-15 instruments.

3.5 Dynamic Calibration: Methods and Results

3.5.1 General Remarks

The calibration methods described in Section 3.4 apply to sensors at rest with respect to the air and are a necessary step in the extraction of accurate data from airborne measurements. However, the physics of the situation becomes much more complex once the aircraft flies and the increased complexity forces the adoption of approximate calibration models. The purpose of dynamic calibration methods is to arrive at the best estimates for the empirical parameters contained in these models. The focus here is entirely on deriving corrections to the measured air temperature, total pressure, static pressure and angles of attack and sideslip required because of imperfect sensor response and flow distortion around the aircraft.

Two dynamic calibration methods were used to estimate the corrections. The first of these was a dedicated calibration flight involving manoeuvres designed to change the environment of a single sensor and provide data on the response of the sensor to this change. The second method used data collected during flights in the 1995 OASIS experiment to optimise the results derived from the calibration flight.

The measurement of the ambient wind field using airborne instruments is described in Lenschow (1986), Lenschow and Spyers-Duran (1989), Leise and Masters (1991) and Williams and Marcotte (2000). The ambient wind field is derived from data measured by airborne instruments using the wind equation (Lenschow, 1986):

$$\mathbf{U}(t) = \mathbf{U}_{GS}(t) - \mathbf{U}_{TAS}(t) \qquad 3.1$$

where $\mathbf{U}(t)$ is the ambient wind field, $\mathbf{U}_{GS}(t)$ is the ground speed of the aircraft and $\mathbf{U}_{TAS}(t)$ is the true airspeed of the aircraft. All quantities are expressed in the Earth coordinate system.

Embodied within this seemingly simple equation is a wealth of difficult detail. Both of these numbers are large, about 40 m s^{-1} in the case of *HNK*, compared to the magnitude of the ambient wind field. The problems of determining the ambient wind become clear as soon as a desired accuracy, say ± 0.5 m s^{-1} for the horizontal

components, is specified. To achieve this, assuming an equal contribution from both quantities in Equation 3.1, means that the aircraft velocity and the relative wind must be known to better than 0.5%. In practice, accuracy of this order or better is possible when measuring the aircraft velocity with an inertial navigation system (Lenschow and Spyers-Duran, 1989) but measurement of the relative wind to the required accuracy demands careful calibration of the aircraft instruments and the optimisation of these from in-flight calibration procedures.

The measurement of the ambient wind field using airborne instruments on *HNK* is described in Isaac and Hacker (2004). These authors present the equations used to derive the ambient winds, develop simplifications of these for special cases to illustrate the important quantities and present a model for the calibration of airborne wind measurements based on the work of Leise and Masters (1991). The flight patterns needed to provide the data required by the calibration model are described and algorithms for estimating the calibration parameters are presented. The following sections in this chapter present the calibration model, describe the flight used to provide data for the calibration of the *HNK* wind measurement instruments according to this model and present the results of the calibration analysis.

3.5.2 Calibration Model

To simplify the process of calibration and provide a convenient starting point, it is assumed that the aircraft ground speed, the first term on the right hand side of Equation 3.1, is already known with sufficient accuracy. Note that this also implies that the aircraft attitude angles, pitch (θ), roll (ϕ) and heading (or yaw, ψ), are accurately known. In practice, on *HNK*, this means that high frequency data on the aircraft velocity and attitude available from the AHS-85 are merged with slower but more stable data from GPS and that the merged data stream has the best characteristics of both sources. This assumption is seldom tested but some aspects are discussed in Section 3.6.2.

With the assumption that $\mathbf{U}_{GS}$ is accurately known, calibration of the wind instruments reduces to calibrating those instruments used to measure $\mathbf{U}_{TAS}$. These are the 5-hole probe, which measures the total pressure and the angles of attack and

side slip, the static pressure sensor and the total temperature sensor. Throughout this section, the term "total" will be prefixed to a quantity to refer to a measurement by a perfect sensor moving through the atmosphere with a speed equal to the true airspeed of the aircraft. The term "static" will be prefixed to a quantity to refer to the measurement of that quantity by a perfect sensor at rest with respect to the atmosphere. When it is necessary to account for the imperfection of a particular sensor, the term "measured" will be prefixed to the quantity derived from this instrument.

The model used to recover $\mathbf{U}_{TAS}$ follows Leise and Masters (1991). The equations are repeated here to provide the context for the discussion of the calibration flights:

$$q_c = K_q q_{c,m} \tag{3.2}$$

$$p_s = p_{s,m} + K_p q_{c,m} \tag{3.3}$$

$$P_\gamma = \left(\frac{p_s}{p_s + q_c} \right)^{\gamma - 1/\gamma} \tag{3.4}$$

$$T_t = \frac{T_{t,m}}{1 - K_T \left(1 - P_\gamma\right)} \tag{3.5}$$

$$T_s = P_\gamma T_t \tag{3.6}$$

$$\tau = \sqrt{2 c_p \left(T_t - T_s\right)} \tag{3.7}$$

where q_c is the dynamic (total minus static) pressure, p_s is the static pressure, T_t is the total temperature, T_s is the static temperature and τ is the magnitude of the true airspeed. The subscript m is used to identify measured quantities, which appear on the right hand side, and to distinguish between these and the same quantities corrected for sensor imperfections by the application of the empirically derived quantities K_q, K_p and K_T. Note that $K_T = 1 - r$ where r is the temperature sensor recovery factor. The remaining terms in Equations 3.2 to 3.7 are the specific heat of air at constant pressure, c_p, and Poisson' s constant, $\gamma = c_p / c_v$ where c_v is the specific heat of air at constant volume.

The magnitude of the true airspeed is resolved into components in the aircraft frame of reference using the angles of attack, α, and sideslip, β. The model equations used to derive these from the pressure differences measured between opposite ports on the 5-hole probe are:

$$\alpha = K_\alpha \frac{\Delta p_\alpha}{q_c} + \alpha_0 \qquad 3.8$$

$$\beta = K_\beta \frac{\Delta p_\beta}{q_c} + \beta_0 \qquad 3.9$$

where Δp_α and Δp_β are the pressure differences measured across the α and β ports respectively, q_c is the dynamic pressure and K_α, K_β, α_0 and β_0 are empirically derived calibration constants. The small-angle approximations $\alpha \approx \tan\alpha$ and $\beta \approx \tan\beta$ have been used in writing Equations 3.8 and 3.9.

The calibration model for $\mathbf{U}_{TAS}$ described above has two powerful features. First, the measured temperature and static pressure can be corrected for changes in the aircraft height when the calibration manoeuvres are performed within the range of the radar altimeter (800 m for *HNK*). Second, the true airspeed in the definition of K_T can be replaced by the ground speed when data from equal duration runs at the same airspeed, and oriented directly into and out of the wind, are averaged. Ground speed is available with good accuracy from the combination of AHS-85 and GPS data. This substitution allows K_T to be estimated from the measured temperatures and ground speed alone, without recourse to the measured pressures.

Use of Equations 3.2 to 3.9 reduces the calibration of $\mathbf{U}_{TAS}$ to determining the empirical constants K_q, K_p, K_T, K_α, K_β, α_0 and β_0. The following section describes a calibration flight designed to provide data for estimating these constants and presents the results from this flight.

3.5.3 Calibration Flight Pattern

The calibration flight took place over Lake Alexandrina, a large shallow lake at the mouth of the Murray River approximately 100 km south-east of Adelaide on 10

October 1996. The location was chosen so that the flight could be performed over water to minimise the horizontal temperature gradient and to ensure a flat surface beneath the aircraft so that the aircraft height could be determined from the radar altimeter. Safety requirements precluded operating the aircraft at low level over the open ocean.

Data for estimating K_T, K_p, K_q and K_α come from 5 pairs of reverse heading runs at airspeeds of approximately 25, 30, 35, 40 and 45 m s^{-1}. The reverse heading runs were oriented directly into and directly out of the mean wind and each run lasted for 5 minutes. All reverse heading runs were done at 160 m. Data for estimating K_β came from 1 pair of reverse heading runs directly into and directly out of the mean wind during which the aircraft was yawed $\pm 10°$ from side to side with as little variation in pitch and roll as possible. These runs were done with an airspeed of 35 m s^{-1}, the typical data collection airspeed for *HNK*, and each lasted for 5 minutes.

In addition to the calibration runs designed to provide the data required for estimating the empirical constants, the aircraft also performed several manoeuvres to allow testing of the calibration. The first of these consisted of a pair of reverse heading runs oriented as before, where the engine power was increased and decreased while the airspeed was held as constant as possible. This caused the aircraft to ascend and descend about the mean height and was designed to vary the vertical component of the aircraft velocity without significant variation of the wing loading.

The second manoeuvre consisted of another pair of reverse heading runs, one directly into the wind and the other directly out of the wind, where the vertical component of the aircraft velocity was modulated by using the elevator control to climb and descend around the mean height. This was designed to test the calibration by comparing the size of any residual in the derived vertical wind with the aircraft vertical velocity.

Finally, the aircraft flew two square patterns ("wind squares"), one clockwise and the other anticlockwise, with the four sides of the square on headings of west, north, east and south. The wind squares were flown at an altitude of 160 m and airspeed of 35 m s^{-1}. Wind squares flown by the FIAMS research aircraft have been the

traditional method used to estimate a correction to the true airspeed that minimises the variation in the horizontal wind components between the four sides of the pattern.

3.5.4 Calibration Flight Results

3.5.4.1 Temperature Sensor Recovery Factor

The starting point for the calibration model is the estimation of the temperature sensor recovery factor because, by careful choice of data, K_T can be estimated without using any of the measured pressures.

K_T is estimated from small differences in the measured temperature due to changes in the airspeed of the aircraft. Temperature changes due to changes in the aircraft altitude must be removed before those due to changes in airspeed can be recovered accurately. This is done by correcting the measured temperature to the mean height of the runs using the environmental lapse rate and the aircraft altitude from the radar altimeter. Use of the radar altitude avoids introducing errors from the uncorrected static pressure.

Problems with the cold junction measurement used by the Meteolabor thermocouple, described in Section 3.7.3, meant that the air temperature derived from this sensor was not stable enough to allow estimation of the instrument recovery factor. The recovery factor estimates for the reverse flow PT100 are given in Table 3.5 for pairs of runs where the difference in airspeed is greater than 10 m s^{-1}.

The estimates show a great deal of scatter and some of the run pairs give estimates of the recovery factor that are greater than unity. This is not excluded by the definition of the recovery factor but it is inconsistent with the assumption that the measured total temperature is less that the actual total temperature due to heat loss from the air as the flow decelerates through the sensor housing. The large scatter and values of r greater than unity are most likely due to the significant temperature variations, about 0.2°C, during the runs even after correction for changes in the aircraft altitude. A value of 1.0 has been used for the reverse flow PT100 recovery factor; this is equivalent to assuming that no correction is required to the measured total temperature.

Table 3.5 Recovery factor, r, and $K_T = 1 - r$ estimates for the reverse flow PT100 based on data from reverse heading runs at different airspeeds. Superscripts *hi* and *lo* refer to the high and low airspeed runs respectively.

Pair	Airspeeds m s^{-1}	$T_{t,m}^{hi}$ °C	$T_{t,m}^{lo}$ °C	U_{GS}^{hi} m s^{-1}	U_{GS}^{lo} m s^{-1}	r	K_T
1	25 & 35	23.41	23.18	36.92	26.86	0.70	0.30
2	25 & 40	23.63	23.18	41.77	26.86	0.88	0.12
3	25 & 45	23.88	23.18	46.07	26.86	1.00	0.00
4	30 & 40	23.63	23.29	41.77	32.88	1.03	-0.03
5	30 & 45	23.88	23.29	46.07	32.88	1.13	-0.13
6	35 & 45	23.88	23.41	46.07	36.92	1.24	-0.24
					Average	**1.0**	**0.0**
					Standard deviation	**0.2**	**0.2**

3.5.4.2 Static and Dynamic Pressure Corrections

The next step in the calibration of the true airspeed measurement is to estimate the dependence of the static pressure measurement on the airspeed. This must be done before the correction to the dynamic pressure is estimated to remove airspeed dependent errors from the total pressure. The model for correcting the measured static pressure, Equation 3.3, assumes that errors in this measurement arise from flow deformation around the aircraft and that these errors are related to the wing loading, or equivalently, the angle of attack. Measured dynamic pressure is used as an analogue for airspeed and, hence, the angle of attack.

As with the recovery factor, the correction is estimated from small differences in the measured static pressure caused by changes in the airspeed of the aircraft. Pressure changes due to changes in the aircraft altitude must be removed before those due to changes in airspeed can be recovered accurately. This is done by correcting the measured pressure to the mean height of the runs using the hydrostatic approximation and the aircraft altitude from the radar altimeter.

The dependence of the measured static pressure on the airspeed, K_p, was estimated using the same set of reverse heading runs used to derive the value of K_T. The results are presented in Table 3.6 for run pairs where the differences in airspeed are greater than 10 m s^{-1}. Pairs 1 and 6 have been excluded from the overall average and standard deviation.

Table 3.6 Estimates of the static pressure correction, K_p, based on data from reverse heading runs at different airspeeds. Superscripts *hi* and *lo* refer to the high and low airspeed runs respectively.

Pair	Airspeeds m s^{-1}	$p_{s,m}^{hi}$ hPa	$p_{s,m}^{lo}$ hPa	$q_{c,m}^{hi}$ hPa	$q_{c,m}^{lo}$ hPa	K_p
1	25 & 35	992.910	992.815	7.67	4.03	*0.026*
2	25 & 40	992.650	992.815	10.19	4.03	-0.027
3	25 & 45	992.525	992.815	12.71	4.03	-0.033
4	30 & 40	992.650	992.775	10.19	5.79	-0.028
5	30 & 45	992.525	992.775	12.71	5.79	-0.036
6	35 & 45	992.525	992.910	12.71	7.67	*-0.076*
					Average	**-0.031**
					Standard deviation	**0.004**

With the exception of pairs 1 and 6, both of which involve runs with a nominal airspeed of 35 m s^{-1}, there is little scatter in the estimates of K_p. The reason for the anomalous values of K_p for these runs was not investigated.

With estimates of K_T and K_p available, it remains to estimate the correction for the measured dynamic pressure, K_q, in order to complete the calibration model for the true airspeed. The value of K_q is estimated using the same set of reverse heading runs used to derive K_T and K_p by iterating around K_q to minimise:

$$e\left(K_q\right) = \left|U_{GS} - \tau\right| \qquad 3.10$$

where U_{GS} is the ground speed and τ is the airspeed, both averaged over equal duration segments into and out of the wind. The results are shown in Figure 3.1 and Table 3.7.

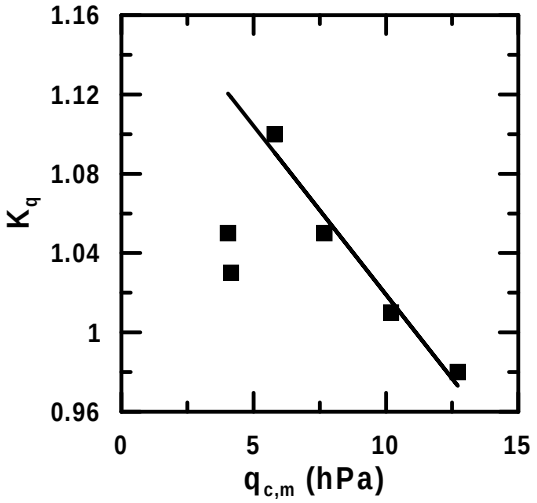

Figure 3.1 Dynamic pressure correction, K_q, versus measured dynamic pressure, $q_{c,m}$. Solid line is Equation 3.11.

The K_q values for runs with airspeeds from 30 to 45 m s^{-1} are well described by:

$$K_q = 1.189 - 0.017 q_{c,m},\ r^2 = 0.970 \qquad 3.11$$

where $q_{c,m}$ is the measured dynamic pressure. Note that the values of K_q estimated from runs 1 and 6, airspeed of 25 m s^{-1}, do not lie on this line. This suggests that the flow around the 5-hole probe at low airspeeds and high (4 to 5°) angles of attack is substantially different from the flow at airspeeds of 30 m s^{-1} and greater.

Table 3.7 Estimates of the dynamic pressure correction, K_q, based on data from reverse heading runs at different airspeeds. The K_q Fit values are derived using Equation 3.11.

Run	Airspeed m s^{-1}	$q_{c,m}$ hPa	K_q	K_q Fit
1	25	4.03	1.05	1.12
2	30	5.79	1.10	1.09
3	35	7.67	1.05	1.06
4	40	10.19	1.01	1.02
5	45	12.71	0.98	0.97
6	25	4.15	1.03	1.12

3.5.4.3 Angles of Attack and Side Slip

It remains to estimate the sensitivities, K_α and K_β, of the angles of attack and sideslip. Data for estimating K_α come from the same reverse heading runs at different airspeeds used to estimate K_T, K_p and K_q. The angle of attack is equal to the aircraft pitch, in straight and level flight and averaged over several minutes, and this allows the aircraft pitch to be used in place of the angle of attack in Equation 3.8. The average angle of attack, and hence the aircraft pitch, can be modulated by varying the airspeed. There is no requirement to average data from the into-wind and out-of-wind runs and these can be used to provide independent estimates of K_α. Data for estimating K_β come from two yaw manoeuvres, one into the wind and the other out of the wind, where the aircraft heading is varied by ±10° about the mean with a period of several seconds. This modulates the drift angle, the angle between the aircraft heading and track, which is equivalent to the angle of sideslip. The aircraft drift angle is available from the combined AHS-85 and TANS GPS data and can be used in Equation 3.9 to provide the sideslip calibration. Once again, into- and out-of-wind runs provide independent estimates of K_β.

The results of the flow angle calibrations are shown in Figure 3.2 and listed in Table 3.8. Data from the out-of-wind runs at 35 and 40 m s^{-1} in the angle of attack calibration deviate significantly from the into-wind points. The reason for this is not known. The separation of into-wind and out-of-wind points in the sideslip calibration shows that the offset, β_0, can not be determined from this data. Methods for estimating the angle of attack and sideslip offsets are discussed in Section 3.6.3. The non-linearity at the extremes in the sideslip calibration, see Figure 3.2b, occur because the pressure difference at high drift angles, >10°, exceeds the dynamic range of the sensor. Sideslip angles of this magnitude are unlikely to occur during data collection runs.

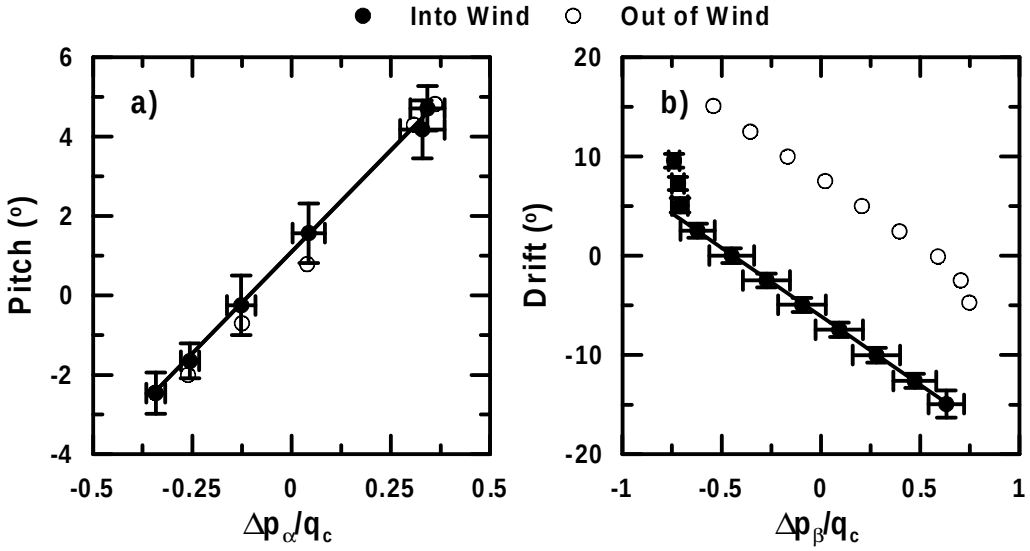

Figure 3.2 Pressure difference normalised by dynamic pressure across a) the angle of attack ($\Delta p_\alpha / q_c$) and b) the angle of sideslip ports ($\Delta p_\beta / q_c$) as functions of aircraft pitch and drift respectively. Error bars are ± one standard deviation; solid line is the line of best fit to the into-wind data.

3.5.4.4 Summary of Calibration Flight Results

The results of the calibration flight are summarised in Table 3.8 along with the historic values used prior to this calibration. Previous calibration models used with *HNK* did not include corrections for the static and dynamic pressures. The estimation of the flow angle offsets, α_0 and β_0 is discussed in Section 3.6.3.

Table 3.8 Values of the calibration coefficients derived from the flight on 9 October 1996 compared to the previous values.

	K_T	K_p	K_q	K_α	K_β
New	0.0 ± 0.2	-0.031 ± 0.004	$1.189 - 0.017 q_c$	10.5 ± 3	-13.8 ± 2
Old	0.07	-	-	9.40	-13.45

3.6 Optimisation of the Wind Measurement Calibration

3.6.1 General Remarks

The preceding sections have described the static and dynamic calibration methods used for the meteorological instruments on *HNK*. This section discusses two areas where in-flight data are used to optimise aspects of the wind measurement calibration.

3.6.2 Phase Differences in Aircraft Data

The calculation of the wind vector from airborne measurements uses data from several sources. For *HNK*, the data required come from the AHS-85, the GPS and five analogue instruments, all of which are sampled and recorded by the data logger at different rates and all of which have different response times. Phase differences between the AHS-85, GPS and analogue data can cause errors in the wind data calculated from airborne instruments (Leise and Masters, 1991; Tjernstrom and Samuelsson, 1995).

The phase differences between the AHS-85, GPS and analogue data were investigated by calculating the correlation coefficient between pairs of quantities at different time lags. Those of greatest interest are between the AHS-85 and GPS velocity components and attitude angles and between these and the analogue data used to calculate the true airspeed vector. Phase differences between the AHS-85 and TANS GPS measurements of the attitude angles are examined first because these are required to rotate the velocity components from the AHS-85 and the GPS to a common frame of reference. A symmetric high-pass filter (cutoff 0.02 Hz) was used to remove long wavelength trends from all data so that these would not dominate the correlation calculation.

The average phase differences between the AHS-85 and the TANS GPS measurements of the aircraft pitch, roll and heading are given in Table 3.9.

Table 3.9 Phase differences between AHS-85 and TANS GPS measurements of pitch (θ), roll (ϕ) and yaw (ψ). Positive values indicate that the TANS GPS lags the AHS-85, uncertainties are plus and minus one standard deviation.

θ Lag s	ϕ Lag s	ψ Lag s
0.6±0.1	0.6±0.1	0.6±0.3

The TANS GPS data lag behind the AHS-85 data by 0.6 s. The difference is the same for all three angles and the scatter in the observed values is small. The average data rate for the TANS GPS during the 1995 OASIS experiment was 1.5 Hz, which corresponds to a period of 0.67 s, close to the observed lag between the TANS GPS and the AHS-85. A faster TANS GPS unit with a data rate of 10 Hz was fitted to *HNK* after the 1995 OASIS experiment and similar tests with this unit revealed a lag of only 0.1 s. These results suggest the observed lags are related to the latency, or calculation time, of the TANS GPS unit.

The aircraft velocity components in Earth coordinates are obtained from the AHS-85 by integration of the accelerations in aircraft coordinates followed by rotation to the Earth frame of reference using the corrected pitch, roll and heading. The phase difference between the aircraft vertical velocity component derived from the AHS-85 and from the time rate of change in pressure altitude (w_{p_a}) was also calculated. w_{p_a} is used to remove drift in the AHS-85 data because large errors can occur in the vertical velocity from the GPS (w_{GPS}) due to poor solution geometry. The average phase differences between the velocity components are listed in Table 3.10.

Table 3.10 Time lags between AHS-85 and GPS ground speed components, u_{GS} and v_{GS}, AHS-85 and GPS vertical velocity component, w_{GPS} and AHS-85 and vertical velocity component from pressure altitude, w_{p_a}. Positive values indicate that the GPS lags the AHS-85; uncertainties are ± one standard deviation.

u_{GS} Lag s	v_{GS} Lag s	w_{GPS} Lag s	w_{p_a} Lag s
2.1±0.4	2.1±0.5	2.0±0.1	0.00±0.05

Aircraft velocity components from the GPS lag behind the AHS-85 data by 2.1 s on average. In contrast, no phase difference was observed between the vertical velocity components derived from the AHS-85 and the pressure altitude.

It is somewhat more difficult to investigate phase differences between the AHS-85 data and the analogue data used to derive the true airspeed of the aircraft. Tjernström and Samuelsson (1995) report such an analysis of phase lags between an Inertial Navigation System (INS) and other data collected on a twin-engine jet aircraft. However, their approach was to iterate over a range of lags between several pairs of INS and analogue data and then choose the set of lags that minimised the variance in the ambient wind velocity components. This approach is not considered suitable for a light, slow moving aircraft such as *HNK*, since over-estimating the response of the aircraft to any movement of the air through which it flies will decrease the calculated variance of the ambient wind. In general, any scheme that uses minimisation of variance, or maximising correlation, as a criterion for choosing parameter values should be used with caution. A reduction in the variance, or an increase in the correlation between two quantities, may be due to factors other than phase differences between data streams.

The wind equation, Equation 3.1, suggests that the important phase differences are those between the aircraft ground speed and attitude angles and the true airspeed, the angle of attack and the angle of side slip. Of particular importance are phase differences between the aircraft ground speed and the true airspeed, between the aircraft pitch and attack angles and between the aircraft drift and sideslip angles.

Phase differences between the ground speed (U_{GS}) and the true airspeed (τ) can be estimated from manoeuvres that modulate both, such as pitching motions. When an aircraft pitches nose up, it trades kinetic energy for potential energy and both the true airspeed and the ground speed decrease. The reverse occurs when the aircraft pitches nose down and the aircraft accelerates. This motion modulates both the true airspeed and the ground speed.

Estimating phase differences between the pitch and drift angles and the angles of attack and side slip can be done by calculating the ambient wind with the correction terms for angular rates disabled. When these terms are disabled for data collected

during aircraft pitching and yawing manoeuvres, the calculated wind components will be contaminated by terms proportional to the angular rates and the displacement of the 5-hole probe from the centre of gravity of the aircraft. This contamination arises from the motion of the 5-hole probe and is sensed via the pressure differences across the angle of attack and sideslip ports and via the dynamic pressure. Using this technique, the phase difference between the aircraft heading and the dynamic pressure can be estimated from the lagged correlation between the true airspeed and the yaw rate (ψ'). Likewise, the phase difference between the aircraft heading and the angle of sideslip can be estimated from the lagged correlation between the cross-track component of the wind vector and ψ'. Finally, phase differences between the aircraft pitch and the angle of attack can be estimated from the lagged correlation between the vertical component of the wind vector and the pitch rate (θ').

The results are summarised in Table 3.11. Uncertainties are plus and minus the observed range in lag values between the available runs.

Table 3.11 Phase differences between the true airspeed magnitude (τ), vertical (w) and cross-track (v_{trk}) components of the wind vector and the ground speed (U_{GS}), yaw rate (ψ') and pitch rate (θ') measurements.

τ vs U_{GS}	τ vs ψ'	w vs θ'	v_{trk} vs ψ'
s	s	s	s
0.1 ± 0.05	0.0 ± 0.05	-0.4 ± 0.05	1.5 ± 0.1

The results show no significant phase difference between τ and U_{GS} or between τ and ψ'. The observed phase difference of -0.4 ± 0.05 s between the vertical component of the wind vector and the pitch rate implies a significant phase difference between the pitch angle and the angle of attack measurement. However, the pitch manoeuvre took place in turbulent air and the contamination in w due to the aircraft pitching motion is not always evident in the data. The result for the comparison of the cross-track component of the wind vector and the yaw rate, 1.5 ± 0.1 s, also implies a significant phase difference between the heading and the sideslip measurement. During the manoeuvre from which this data was taken, the aircraft was yawed by $\pm 10°$ about the mean heading and the pressure difference across the sideslip port exceeded the dynamic range of the sensor. This results in

large spikes in the cross-track component of the wind vector and these spikes may have obscured any real phase difference between the aircraft heading and sideslip measurements.

To summarise, the GPS velocity components were found to lag behind those from the AHS-85 by 2.1 s while the GPS attitude angles were found to lag by 0.6 s. No phase difference was observed between the ground speed and the true airspeed magnitudes but the results are inconclusive for the angles of attack and sideslip. In the light of these results, it is reasonable to assume that there is no phase difference between the analogue data and the measurements of aircraft velocity and attitude from the AHS-85. This is further supported by the lack of phase difference between the vertical components of the aircraft velocity derived from the AHS-85 and from the pressure altitude.

3.6.3 Optimisation of Calibration Using Flight Data

Data from flights conducted during 1995 OASIS experiment can be used to check and, if necessary, optimise the calibrations for true airspeed and the angle of sideslip. Optimisation of the angle of attack calibration by fine tuning the value for α_0 is not considered since the only quantity sensitive to this is the mean of the vertical component of the wind vector and this is forced to zero during the data processing. The value of α_0 obtained from the 1996 calibration flight results was used in the processing of the 1995 OASIS aircraft data.

It is worth noting at the outset that the calculated true airspeed is relatively insensitive to both K_T and K_p but is very sensitive to K_q. Sensitivity tests show that varying K_T from 0.0 to 0.30 causes τ to vary by 0.05% for flight conditions typical of *HNK*. Similar results are obtained when K_p is varied from -0.05 to 0.05. Varying K_q from 1.00 to 1.10 causes a 5% change in τ. Changes in τ translate directly into changes in the wind speed for a given aircraft ground speed. The wind direction is predominantly determined by the aircraft heading and the angle of sideslip, β, in particular the β calibration offset, β_0. The sensitivity of the calculated wind direction to errors in β_0 depends on the aircraft heading relative to

the wind direction and on the magnitude of the wind speed. It is greatest when the aircraft flies parallel to the wind and when the wind speed is small. For an aircraft flying parallel to the wind, changing β_0 by $\pm 0.5°$ causes a $\pm 19°$ change in the calculated wind direction when the wind speed is 1.0 m s^{-1} but this drops to $\pm 4°$ when the wind speed is 5.0 m s^{-1}.

If the aircraft is restricted to straight and level flight, then the wind vector components parallel to and perpendicular to the aircraft are given by:

$$\begin{aligned} u_{hdg} &= u_{GS,hdg} - \tau \cos\beta \\ v_{hdg} &= v_{GS,hdg} - \tau \sin\beta \end{aligned} \qquad 3.12$$

where u_{hdg} and v_{hdg} are the components parallel to and perpendicular to the aircraft, $u_{GS,hdg}$ and $v_{GS,hdg}$ are the along-heading and cross-heading components of the aircraft ground speed, τ is the true airspeed and β is the angle of sideslip. For a typical range of sideslip angle, say $\pm 5°$, $\cos\beta$ ranges from 0.996 to 1.000 and $\sin\beta$ ranges from -0.087 to 0.087. This means that the along-heading component of the wind vector is less sensitive to β and proportionally more sensitive to the true airspeed than the cross-heading component. This separation can be used to diagnose problems in the calibration of these quantities and to optimise the calibration coefficients K_q and β_0.

The data for optimising K_q and β_0 comes from consecutive reverse heading runs where the assumption can be made that the wind vector remains constant during the runs. The low-level field and grid patterns from the 1995 OASIS experiment fulfil these criteria. Both consisted of multiple reverse heading runs (10 to 14 for the low-level field pattern and 5 for the grid pattern) and took less than 1 hour to perform (30 minutes and 45 minutes respectively). The optimisation procedure consists of choosing the value of K_q that minimises the variance in u_{hdg} and the value of β_0 that minimises the variance in v_{hdg}.

The results from the optimisation are presented in Table 3.12. Results for K_q are given as K_q^{opt} / K_q^{cal}, the ratio of K_q from the optimisation versus the value from the

calibration flight. A value of 1.0 indicates that the optimisation finds no correction is required to the value of K_q derived from the calibration flight.

Table 3.12 Values of K_q^{opt} / K_q^{cal} and β_0 derived from the low-level field and grid patterns during the 1995 OASIS experiment. Uncertainties are plus and minus one standard deviation.

Day	K_q^{opt} / K_q^{cal}	β_0
16/10/95	1.005	1.0
17/10/95	1.005	1.8
18/10/95	0.998 ± 0.004	0.8 ± 0.4
19/10/95	1.005	0.4
20/10/95	-	-
23/10/95	1.00 ± 0.02	0.9 ± 0.4
24/10/95	1.003 ± 0.007	0.8 ± 0.4
25/10/95	1.004 ± 0.005	0.8 ± 0.3
26/10/95	1.000 ± 0.007	1.0 ± 0.5
27/10/95	0.995 ± 0.006	0.7 ± 0.2
29/10/95	0.996 ± 0.003	0.7 ± 0.3
Average	1.001 ± 0.009	0.8 ± 0.4

The daily values of K_q and β_0 were used in the data processing, though no explanation was found for the day to day variation in these quantities. The uncertainty in K_q^{opt} / K_q^{cal} equates to an uncertainty in the wind speed of 0.4 m s^{-1}. The uncertainty in β_0 equates to an uncertainty of between 3 and 15° in the wind direction depending on wind speed (higher uncertainty at lower wind speeds).

3.7 Known Instrumentation Problems

3.7.1 Dynamic Pressure

The most serious problem encountered with the aircraft instrumentation during 1995 OASIS experiment occurred with the dynamic pressure measurement. On *HNK*, the dynamic pressure is measured as the difference between the total pressure at the centre hole of the 5-hole probe and the static pressure at the ports behind the probe tip.

The pressure sensors in the instrument pod of *HNK* are coupled to their respective ports using silicon tubing (6 mm outside diameter), which is soft and easily deformed. Care is needed when assembling the instrument pod to avoid catching the tubes between the upper and lower halves of the pod casing. If this happens, the tubes can be pinched together or kinked and this may affect the propagation of pressure changes through the tubing leading to errors in the pressure measurements. On 19 October 1995, the pilot of *HNK* remarked that the indicated airspeed displayed on the data logger did not always agree with the indicated airspeed shown on an independent measurement on the instrument panel of the aircraft. Despite this warning, the instrument pod was not checked until the morning of 23 October 1995. Inspection of the pressure lines on this day showed that the tube linking the centre hole of the 5-hole probe (total pressure port) to the dynamic pressure sensor was partially restricted. The tubes were re-located, the pod re-assembled and the response of all pressure sensors checked by blowing into the respective ports and observing the data on the logger display.

The constriction of the tube leading to the dynamic pressure sensor degraded the quality of the dynamic pressure data in two ways. Firstly, fluctuations in the dynamic pressure with periods of less than two seconds were lost from the data record for the first 6 days of the experiment. Figure 3.3 shows spectra of the wind speed, u, weighted by frequency and normalised by the variance, from two flights at 6 m over the wheat crop at the Wattles site. The constriction in the pressure line was removed on 23 October 1995. The fluctuations in u at frequencies greater than 0.07,

a wavelength of approximately 90 m, have been attenuated as a result of the constriction in the tube.

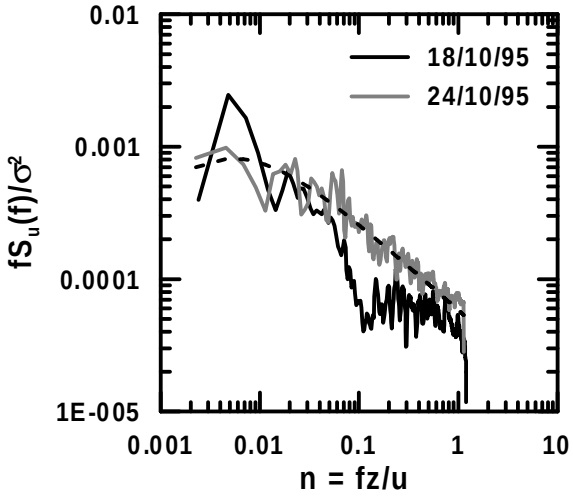

Figure 3.3 Spectra of the horizontal wind speed at 6 m with the constricted dynamic pressure line (18/10/95) and after the line had been freed (24/10/95). Dashed line is the spectral form from Kaimal and Finnigan (1994).

The second effect was to slow the propagation of pressure changes along the tube because air could only bleed slowly from one side of the constriction to the other. This meant that the static pressure side of the dynamic pressure sensor accurately tracked rapid changes but the total pressure side did not. This lead to the sensor interpreting changes in the static pressure, for example when the aircraft was ascending or descending, as changes in the dynamic pressure. This effect is illustrated in Figure 3.4, which shows a section of aircraft data for 12 low-level runs on 19 October 1995.

The aircraft made 12 passes over the fields at 6 m during this flight and landed at an adjacent gliding strip at the completion of the passes. At the end of each pass, the aircraft climbed to approximately 50 m while turning onto the reverse heading for the next pass. The aircraft ascents between each low-level pass are evident in Figure 3.4 as the regular dips in the static pressure.

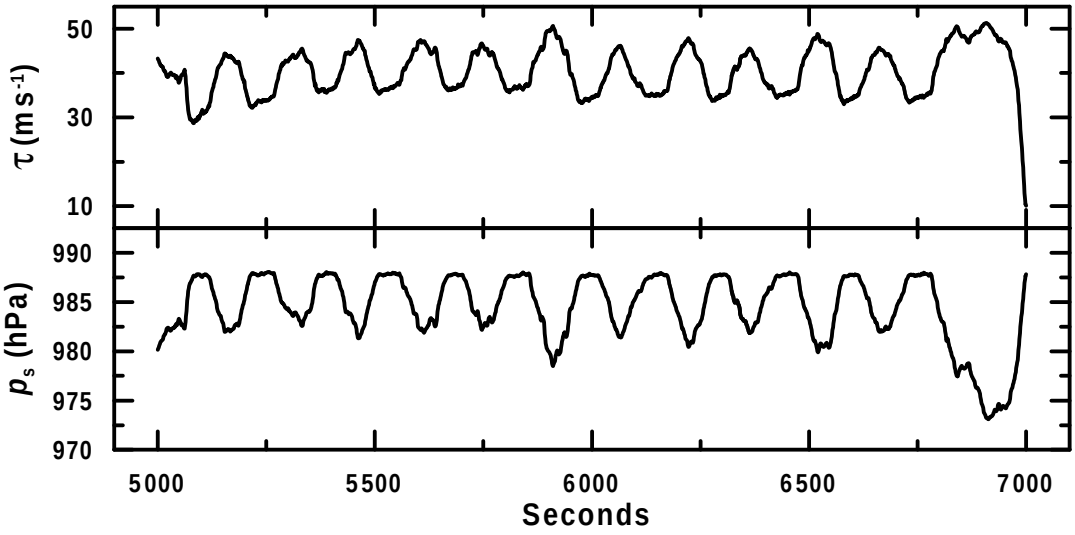

Figure 3.4 Plot of the static pressure (p_s) and true airspeed (τ) for the low-level runs on 19 October 1995. The short sections with $p_s \approx 987.5$ hPa are the low-level passes over the wheat field and the excursions to $p_s \approx 982.5$ hPa are the aircraft turns between passes.

Figure 3.4 shows the true airspeed increasing as the static pressure decreases and decreasing as the static pressure increases, which implies that the aircraft is accelerating as it climbs and decelerating as it descends. This behaviour is not consistent with the modest climb performance of *HNK*, but it is consistent with the total pressure side of the dynamic pressure sensor being unable to respond to rapid changes in the static pressure. Figure 3.4 also shows that the mean value of the true airspeed is correct, about 40 m s^{-1}, even though the true airspeed data appears to be contaminated by a component of the static pressure.

A model for correcting the dynamic pressure for contamination by changes in the static pressure was constructed as follows. Firstly, the correct total pressure at the centre hole of the 5-hole probe is given by:

$$p_t = p_s + q_c \qquad 3.13$$

where p_t is the total pressure, p_s is the static pressure and q_c is the dynamic pressure. The contaminated total pressure measured by the dynamic pressure sensor is:

$$p_t' = p_s' + q_c \qquad 3.14$$

where p_t' and p_s' are the contaminated total and static pressures respectively. The dynamic pressure measured by the sensor is then:

$$q_c' = p_t' - p_s . \qquad 3.15$$

To obtain the correction model, the contaminated static pressure is assumed to be a function of the correct static pressure:

$$p_s' = f(p_s) . \qquad 3.16$$

Combining this with Equations 3.13, 3.14 and 3.15 and rearranging gives:

$$q_c = q_c' + p_s - f(p_s) . \qquad 3.17$$

Equation 3.17 suggests that the correct dynamic pressure can be recovered from the contaminated dynamic pressure and the static pressure if the form of the function $f(p_s)$ can be found. Noting that the mean true airspeed appears to be correct, an estimate of $f(p_s)$ can be made by setting $q_c \approx \overline{q_c'}$ where $\overline{q_c'}$ is the mean of the contaminated dynamic pressure. Substituting this into Equation 3.17 and rearranging gives:

$$f_{est}(p_s) = \left(q_c' - \overline{q_c'}\right) + p_s . \qquad 3.18$$

The quantity $f_{est}(p_s)$ is plotted in Figure 3.5. The comparison with p_s suggests that $f_{est}(p_s)$ is a lagged and attenuated version of the departure of p_s from a long term mean, similar to the results of applying a non-symmetric low-pass filter to p_s.

A recursive, low-pass filter (Kaimal and Finnigan, 1994) was used to approximate $f(p_s)$. The time constant of the filter was chosen to minimise the correlation between q_c and p_s. This is justified on the basis that the correlation between q_c and p_s was either zero or a small positive value for the low-level flights after the fault was corrected. Note that a small positive correlation means that the aircraft decelerates as it climbs and accelerates as it descends.

Figure 3.5 shows the data for the same low-level passes as used in Figure 3.4. There is good agreement between $f_{est}(p_s)$ and the low-pass filtered p_s and the resulting correction to q_c' removes most of the contamination due to the changing static pressure.

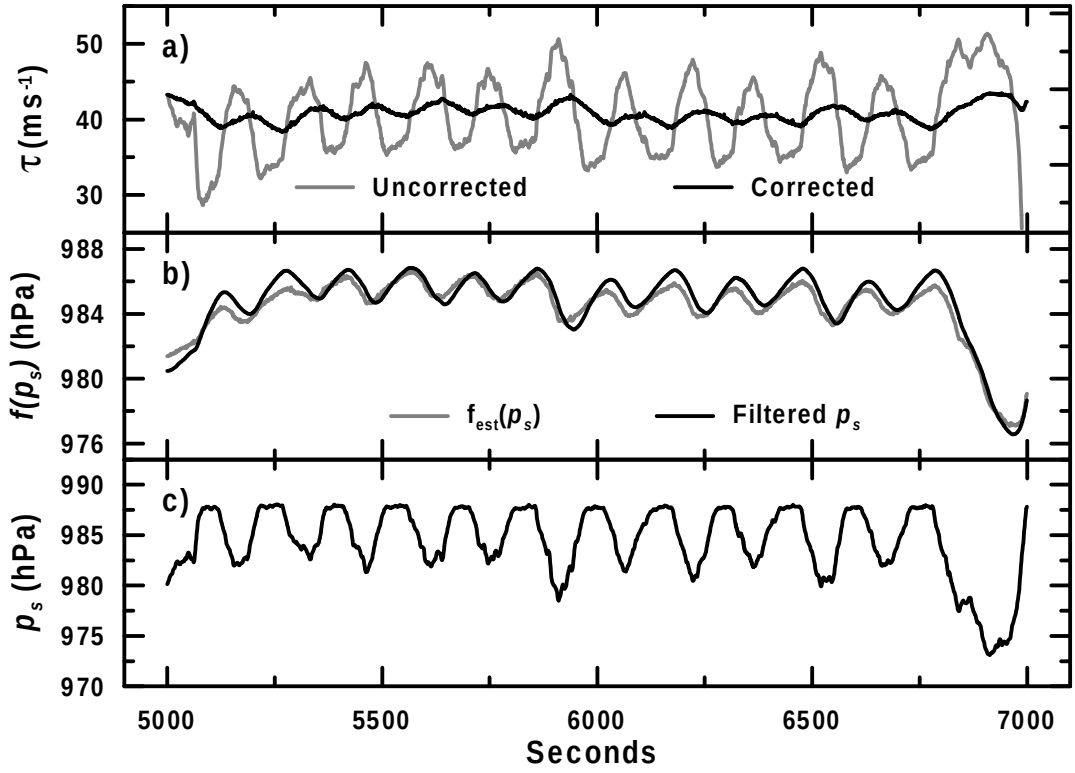

Figure 3.5 Plot of the a) corrected and uncorrected τ, b) filtered p_s and the estimated q_c correction term $f_{est}(p_s)$ and c) the static pressure p_s.

The correction only affects the mean value of the true airspeed, it is not possible to recover the lost turbulence information. This is not significant for vertical scalar fluxes because most of the information on the turbulent part of the vertical velocity component is contained in the angle of attack (Isaac and Hacker, 2004). The likely impact will be on the vertical flux of momentum, which will be underestimated because of the loss of high frequency information in u.

3.7.2 Reverse Flow Response Time

Isaac and McAneney (1997) reported initial results from a comparison of aircraft and ground-based observations during the low-level flights over the wheat fields at the

Wattles site. Their results showed good agreement between the aircraft and ground based measurements of wind speed, U, wind direction, WD, and air temperature, T_a and between the aircraft and ground based measurements of the standard deviations of vertical wind speed, σ_w, horizontal wind speed, σ_u, and specific humidity, σ_q. Aircraft and ground based measurements of the latent heat flux, F_E, also showed good agreement.

In contrast to these results, the aircraft measurements of the standard deviation of temperature, σ_T, and sensible heat flux, F_H, under-estimated the ground based measurements by factors of 1.64 and 2.38 respectively. Figure 3.6 reproduces the relevant figure from Isaac and McAneney (1997). The under-estimation of both σ_T and F_H by the aircraft measurements when σ_w, σ_q and F_E are all in agreement with the ground based data suggests a loss of temperature variance in the aircraft data.

The flow of air around and through the reverse flow housing was investigated by mounting the reverse flow temperature sensor in a small wind tunnel (Defence Scientific and Technical Organisation, Adelaide, Australia). The tunnel had a working cross section of 30 cm by 30 cm and wind speeds in the tunnel could be continuously varied from 0 to 15 m s^{-1} in addition to a high speed mode of 27 m s^{-1}. The airflow through the reverse flow sensor was visualised by injecting oil smoke into the opening at the rear of the housing body. Figure 3.7 is a photograph of the reverse flow housing in the wind tunnel during the flow visualisation test. The silver tube at the rear of the housing is the nozzle of the smoke generator. Grey smoke can be seen leaving the upper arm and travelling a short distance away from the arm before being trapped and directed downwards toward the body of the sensor.

Visualisation of the flow confirmed that air passed through the sensor in the reverse direction to the external flow and was vented through the three radial arms projecting from the body of the sensor. However, the exhaust smoke was trapped in the lee of these arms and transported back towards the body of the housing instead of entering the free stream air and being carried away from the sensor. This leads to the recirculation of air through the sensor as exhaust air exits from the radial arms, returns to the sensor body and gets entrained into the rear opening. The recirculation

of air through the housing increases the sensor response time, and decreases the temperature variance seen by the PT100 sensing element, due to the prolonged contact between the air and the housing body.

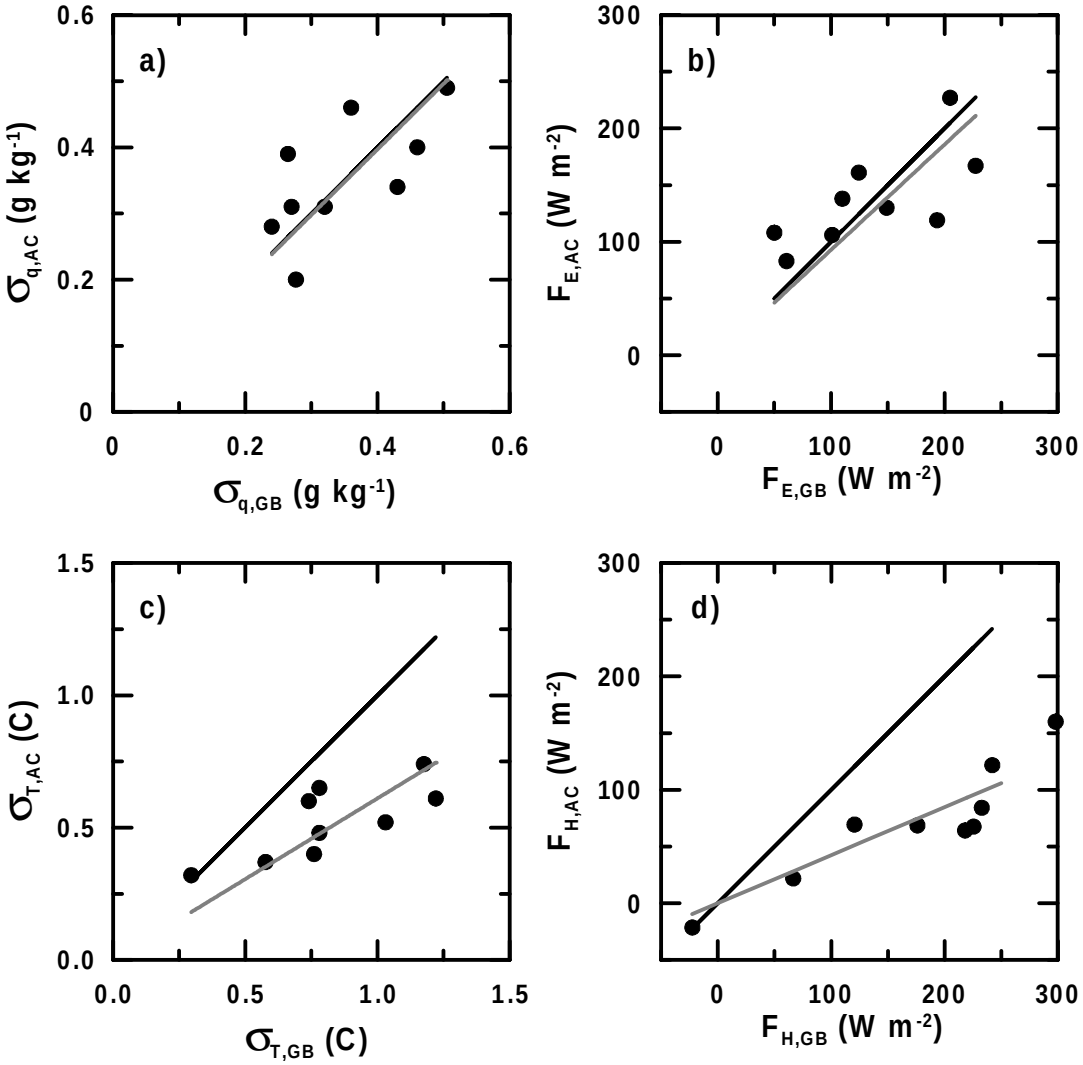

Figure 3.6 Comparison of aircraft and ground based measurements of a) standard deviation of specific humidity σ_q, b) latent heat flux F_E, c) standard deviation of air temperature σ_T and d) sensible heat flux F_H. The black line is 1:1 and the grey line is the line of best fit through the origin. Reprinted from Isaac and McAneney (1997).

Rodi and Spyers-Duran (1972) proposed an empirical model to describe the response of aircraft temperature sensors to a step change:

$$\Theta(t) = \frac{T_m - T_F}{T_I - T_F} = Ae^{-t/\tau_1} + Be^{-t/\tau_2} \qquad 3.19$$

where T_m is the sensor temperature at time t, T_I is the temperature before the step change and T_F is the temperature at infinity, taken to be the temperature at some suitably long time after the step change. τ_1 and τ_2 are the sensing element and housing time constants respectively and the sum of the two coefficients, A and B must be one.

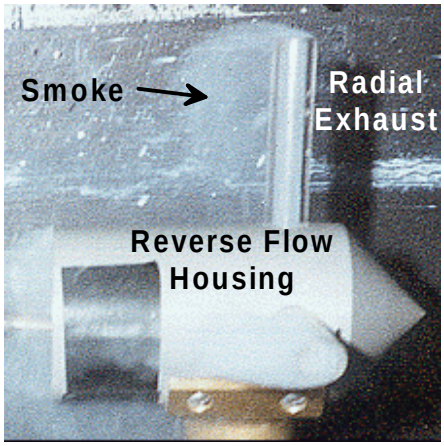

Figure 3.7 Photograph of the reverse flow sensor in the wind tunnel. The nozzle of the smoke generator is the small silver tube at the left edge of the photograph. Smoke can be seen exiting from two of the three radial exhaust arms.

McCarthy (1973a) described a method for correcting temperature data using this model and derived a correction algorithm based on integration of a differential equation containing the first and second derivatives of the measured temperature with time. This method was criticised by Acheson (1973) as "finding the problem to fit a solution" on the basis that the proposed correction algorithm was derived from a description of the sensor response to a particular (step) temperature input but was then applied to the general case. In reply, McCarthy (1973b) admitted that a physical basis for the correction algorithm was lacking but noted that the proposed method had been carefully tested and was "a reasonable substitute to a complete physical model". Payne et al. (1994) attempted to provide a physical model for the Rosemount 102 probe by considering the heat transfer between the platinum wire from which the sensor is wound and the supporting structure over which it is wound.

Their analysis showed that the results of the model can be closely approximated by the two-time constant model, Equation 3.19, but their values of the empirical constants, A, B, τ_1 and τ_2, do not agree with those published by other authors (Rosemount, 1963; Spyers-Duran and Baumgardner 1983; Friehe and Khelif 1992). Further, they note that the lack of agreement suggests their model under-estimates the attenuation of temperature fluctuations by the sensor. This may be due to the fact that their analysis is restricted to heat transfer from the wire to the support structure and does not consider the effect of the sensor housing. Despite these shortcomings, the response function described by Equation 3.19, and the algorithms based on this, remain the only practical means for correcting temperature data affected by long sensor time constants.

Inverarity (2000) uses the same two-time constant model but derives an alternative correction algorithm to that presented by McCarthy (1973a), with the advantages of improved computational accuracy and efficiency. The alternative also avoids using the second derivative of the measured temperature, which can be very noisy when calculated from a discrete time series of turbulence data using a finite difference scheme. The correction method adopted here uses the two-time constant model of Rodi and Spyers-Duran (1972) and the correction algorithm of Inverarity (2000).

The three empirical constants required by the model, τ_1, τ_2 and one of A or B, were estimated from measurements made at the same time as the flow visualisation experiments in the wind tunnel. An unhoused PT100 element (25 μm wire, $\tau_1 < 0.1$ s in still air) was placed alongside the reverse flow temperature sensor near the centre of the working section of the tunnel. Step changes in temperature were simulated by injecting heated air from a commercial hot air gun into the tunnel upwind of the sensors, allowing the sensors to reach equilibrium and then rapidly removing the hot air source. Figure 3.8 shows the data for the bare PT100 and the reverse flow temperature sensor for one wind tunnel run.

Attempts to estimate the required parameters by a least squares fit of Equation 3.19 to the reverse flow data did not result in a single set of values. The values obtained from this procedure were found to be very sensitive to the choice of starting point (T_I) in the data series and to the duration of the segment chosen for the fitting

process (T_F). In addition to these problems, using a segment that was sufficiently long to capture the slow decay tended to reduce the significance of the initial drop and vice versa. Instead, the parameters were estimated by applying the correction algorithm to the temperature data from the reverse flow sensor using a range of values and choosing the set which gave the best fit to the temperature data from the bare PT100 element. This requires the plausible assumption that the time constant of the bare PT100 element is short enough to accurately measure the turbulent fluctuations in T_a but avoids the problems due to temperature fluctuations in the tunnel and a non-ideal shape of the temperature front. Tests were performed at wind speeds of 15 and 27 m s^{-1} but the parameters ($\tau_1 = 0.15$, $\tau_2 = 40$ and $A = 0.7$) showed no dependence on wind speed.

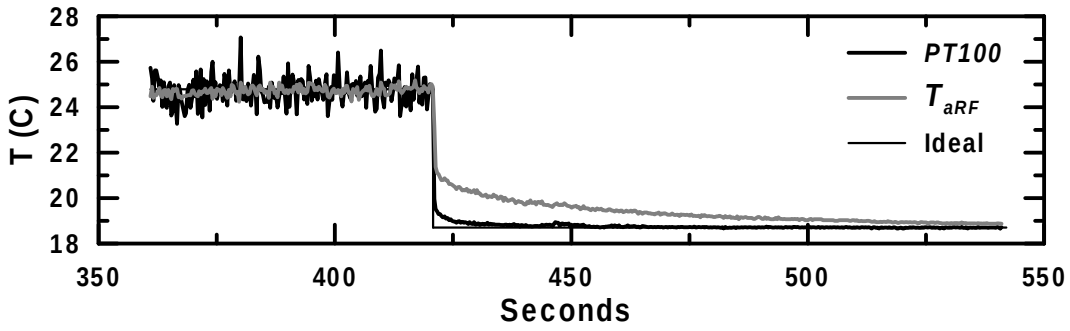

Figure 3.8 Air temperature measured inside the wind tunnel by the bare sensor element ("PT100", black) and by the reverse flow sensor ("T_{aRF}", grey). Also plotted for comparison is an idealised step change ("Ideal", thin black).

Figure 3.9 shows a 10 s segment from the wind tunnel run plotted in Figure 3.8 centred on the temperature change at 420.75 seconds. The corrected reverse flow temperature closely resembles the data from the bare PT100 element.

Use of the correction algorithm with the parameter values listed above increases the aircraft observations of σ_T at 6 m by a factor of two but introduces an unacceptable level of noise into the temperature data at frequencies above 1 Hz. The noise is evident in Figure 3.9 in the jitter of $T_{aRF}(\mathrm{cor})$ about the line for PT100 from 421 seconds onward.

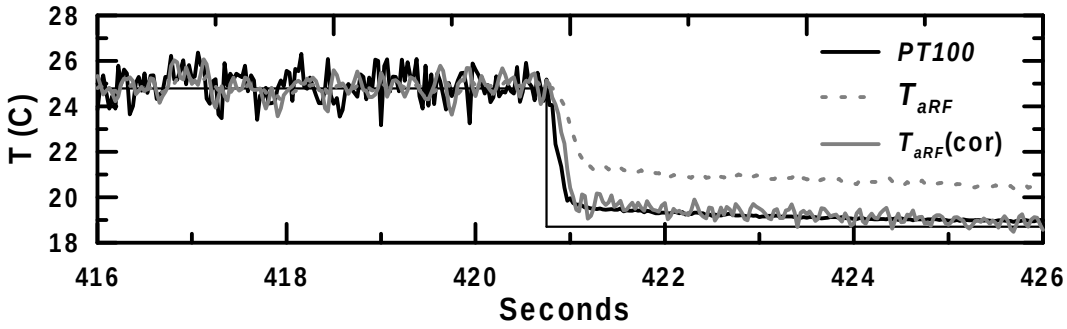

Figure 3.9 A 10 second segment of the wind tunnel run shown in Figure 3.8 centred on the temperature change at 420.75. Plotted are the air temperature measurements by the bare sensor element ("PT100", thick black), the reverse flow sensor ("T_{aRF}", dashed grey) and the corrected reverse flow data ("$T_{aRF}(\mathrm{cor})$", thick grey).

The source of the noise introduced by the correction algorithm was examined by careful inspection of the raw and corrected data. Figure 3.10a shows a 5 s segment of specific humidity, q, corrected temperature, $T_{aRF}(\mathrm{cor})$, and the reverse flow sensor data corrected using a modified algorithm described below, $T_{aRF}(\mathrm{mod})$. The data come from a flight at 6 m over the wheat field at the Wattles site on 24 October 1995 and have been normalised by subtracting the means and dividing the result by the standard deviations to facilitate display on the same axes. Specific humidity is calculated from data recorded by the NOAA IRGA, which has a response time of less than 0.1 s (Auble and Meyers, 1992). The fast response of the open path IRGA and the high correlation between the uncorrected temperature data and q ($r = 0.95$), allow q to be used as a reference for the shape of the corrected temperature. The high frequency noise introduced by the response time correction can be seen in the sharpness of the peaks and troughs in the corrected temperature time series and in the lower correlation between T_a and q ($r = 0.78$). Figure 3.10b and c show the normalised, frequency-weighted power spectra and cospectra for the aircraft flight from which the 5 second segment was taken and the high frequency noise introduced by the correction is clearly evident in both.

Detailed inspection of the three terms in the Inverarity (2000) algorithm showed that the first derivative of the measured temperature was responsible for introducing the high frequency noise into the corrected temperature. The derivative may be noisy or

inaccurate when it is calculated from a discrete time series using a finite difference scheme, if there is noise present in the temperature data to begin with and if the actual response of the instrument differs from Equation 3.19. In order to reduce the effect of this noise, a low-pass filter (Kaimal and Finnigan, 1994) was applied to the derivative in a modification to the correction algorithm. The filter time constant of 0.5 s was chosen to suppress the spurious negative peaks introduced by the correction (eg. at 4624 seconds in Figure 3.10a). No phase difference was found between the uncorrected temperature and the temperature corrected using the modified algorithm.

Temperatures corrected using the modified algorithm (solid black line in Figure 3.10a) follow the specific humidity much more closely than those corrected using the unfiltered derivative (solid grey line) and they also retain the high correlation between T and q ($r = 0.96$). The spectra (Figure 3.10b) show that the high frequency noise introduced by the unmodified correction is almost entirely removed and the cospectrum (Figure 3.10c) of the temperature corrected using the modified algorithm is almost identical to that for specific humidity. For the aircraft flight depicted in Figure 3.10, applying the response-time correction using the filtered temperature derivative increases σ_T by a factor of 1.66 and increases the wT covariance by a slightly higher factor of 1.75. The modified corrections bring the aircraft data very close to results from the fixed towers, see Chapter Four.

This section merits some concluding remarks.

Many comparisons of aircraft and ground based data have shown that the aircraft measurements of F_H under-estimate those from ground based sites while the F_E comparisons are usually much more favourable (Shuttleworth, 1991). It seems plausible that some of this disagreement may be due to an inadequate response time of the temperature sensor, particularly since the effect of a slow response time is not always evident in the temperature spectra. Spectra of the uncorrected temperature from the reverse flow sensor on *HNK* showed little sign of the effect of a long sensor response time and were in good agreement with humidity spectra from a fast response absorption instrument. The explanation lies in an ambiguity in interpretation of the Fourier transform used to compute the spectral estimates.

Increasing the amplitude of narrow peaks that are widely spaced results in an increase in spectral power at both long and short wavelengths. This increase is indistinguishable from that caused by an increase in the amplitude of either long, or short, wavelength features in the time series.

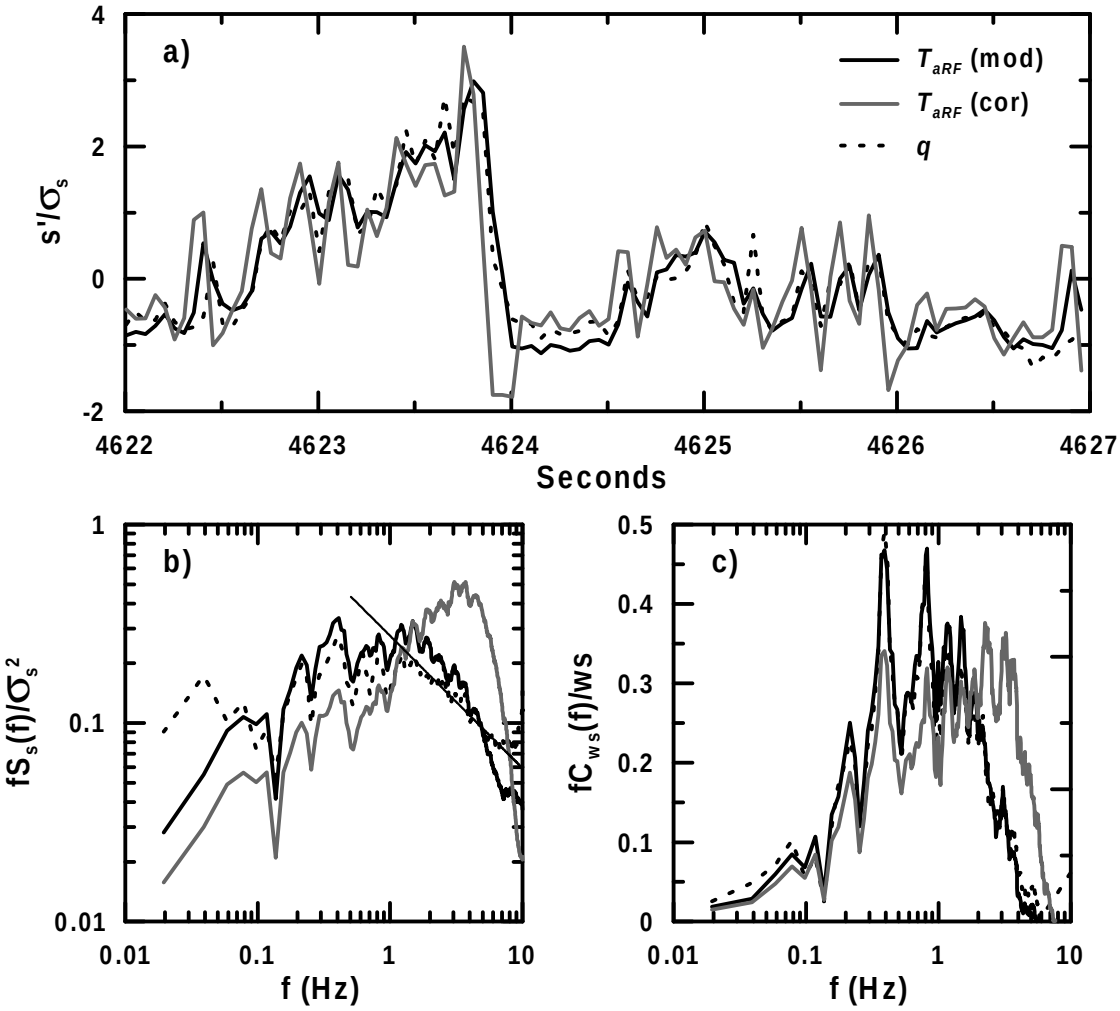

Figure 3.10 a) Time series, b) spectra and c) cospectra with w of specific humidity ("q", dashed line), corrected reverse flow data ("$T_{aRF}\left(\mathrm{cor}\right)$", solid grey line) and reverse flow data corrected with the modified algorithm ("$T_{aRF}\left(\mathrm{mod}\right)$", solid black line). The $f^{-5/3}$ dependency is plotted as a thin black line in b). The data were recorded by the aircraft instruments at 6 m above the wheat field at the Wattles site.

Finally, the model used for the response time correction is empirical, estimation of the required parameters is not robust and although the resulting correction is very powerful, it is limited by the fidelity of the measured temperature. Said differently,

the correction can not recover all of the information lost due to averaging by the sensor but will happily amplify noise in the belief that all fine structure is real. In conclusion, it is much better to build a faster sensor than to attempt correction of contaminated data from a slow response instrument.

3.7.3 Meteolabor Reference Temperature

Comparison of the air temperatures measured by the Meteolabor thermocouple and the FIAMS PT100 showed differences of 1 to 3°C between the observations, even after applying the calibrations described earlier. The difference was not constant but tended to vary throughout an aircraft flight. A similar difference was found between the Meteolabor dew point temperature and the dew point calculated from the NOAA IRGA measurement of absolute humidity. These systematic differences were not found during the calibration runs in the environmental chamber where the Meteolabor air temperature measurements showed good agreement with those from an HP2801 quartz thermometer and the dew point measurements agreed with those from a LICOR 6262 gas analyser. The Meteolabor unit was removed from the aircraft instrument pod during these calibrations. An offset of 2 to 3°C was found between the LICOR 610 Dew Point Generator setting and the Meteolabor dew point during in-situ calibrations with the Meteolabor mounted in the pod and the pod mounted on the aircraft. This suggests that the offset may be related to the installation of the Meteolabor in the instrument pod.

The thermocouples used to measure the air and dew point temperatures are mounted 0.5 and 0.25 m respectively from the processing electronics in the instrument pod. Following accepted instrumentation practice, conductors of the same type as the thermocouple junction (copper/constantan) are used to connect the sensors to the processing electronics but these wires are terminated at a DB25 plug outside the box housing the electronics. From this point, standard copper conductors are used to connect the DB25 socket to the printed circuit board of the electronics. The reference thermistor used as the thermocouple cold junction temperature is mounted on the circuit board of the processing electronics. The use of copper conductors to connect the thermocouples to the electronics means that the actual cold junction occurs in the DB25 socket and not at the edge of the circuit board containing the

reference thermistor. This results in the cold junction measurement and the actual cold junction being physically and thermally separate. The heat dissipated by the electronics inside the box causes the reference temperature to be greater than the actual cold junction temperature outside the box. In addition to this, changes in the air temperature will change the temperature inside the instrument pod and are likely to affect the actual cold junction more than the reference temperature due to the insulation offered by the box housing the Meteolabor electronics.

The reverse flow PT100 has been used as the primary air temperature measurement during the 1995 OASIS experiment. To reduce the effect of the incorrect cold junction measurement on the absolute humidity derived from the Meteolabor, the relative humidity is calculated using the Meteolabor air and dew point temperatures and the absolute humidity is then calculated from this and the air temperature from the reverse flow PT100.

3.7.4 CO_2 Measurements by NOAA IRGA and LICOR 6251

CO_2 concentration measurements were made using both open-path (NOAA IRGA) and closed-path (LICOR 6251) instruments on *HNK* during the 1995 OASIS experiment. The intention was to use data from the NOAA IRGA to provide measurements of the turbulent fluctuations in CO_2 concentration while data from the LICOR 6251 provided measurements of the absolute CO_2 concentration. Figure 3.11 shows spectra of specific humidity and CO_2 measured by the NOAA IRGA and CO_2 measured by the LICOR 6251 and cospectra with vertical velocity for specific humidity measured by the NOAA IRGA and CO_2 measured by the LICOR 6251. Specific humidity measured by the NOAA IRGA is used here as a scalar tracer and, assuming spectral similarity for H_2O and CO_2, provides examples of spectra and cospectra that are uncontaminated by instrumental problems.

The NOAA IRGA CO_2 spectrum shows a continuous increase in power for frequencies greater than $n = 0.03$, which is characteristic of white noise in the raw data (Kaimal and Finnigan, 1994). Close examination of time series of the NOAA IRGA CO_2 data showed that the noise consisted of apparent fluctuations in the CO_2 concentration with periods of the order of a second and amplitudes of the order of 2 to 3 mg m^{-3}. Attempts to remove the noise using a simple recursive filter (Kaimal

and Finnigan, 1994), an enhanced triangle filter (Leise and Masters, 1991) and a Savitsky-Golay filter (Press et al., 1992) were unsuccessful and the NOAA IRGA CO_2 measurements were rejected for further analysis.

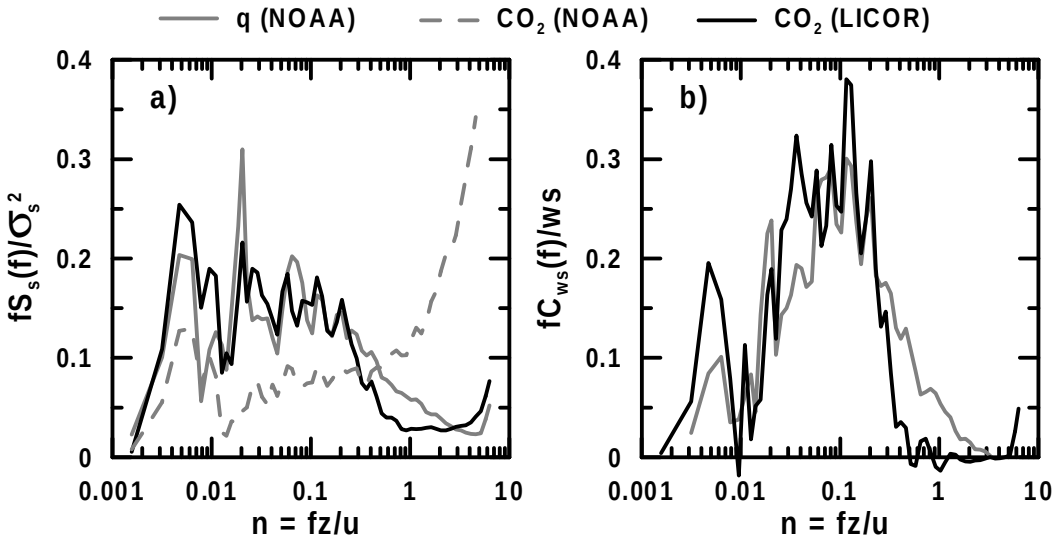

Figure 3.11 Plots of a) spectra of specific humidity and CO_2 concentration from the NOAA IRGA and CO_2 concentration from the LICOR 6251 and b) cospectra with vertical velocity of specific humidity from the NOAA IRGA and CO_2 concentration from the LICOR 6251. The data were collected at 26 m during a 10 km segment of the transect centred on the Browning site.

The LICOR 6251 CO_2 measurements suffered from two problems. The most serious of these was the attenuation of high frequency information in the CO_2 concentration measurements, see Figure 3.11. The reasons for the attenuation and the steps taken to correct for this are described later in this section. The second problem was the time lag in the LICOR 6251 CO_2 measurements due to the volume of the inlet tube and the sample cell and the flow rate through the LICOR 6251.

The inlet tube to the LICOR 6251 was a 1.5 m length of Teflon tubing with an internal diameter of 4 mm, giving a tube volume of 18.9 cm^3. The dimensions of the LICOR 6251 sample cell are 0.6 x 1.3 x 15.2 cm, giving a sample cell volume of 11.9 cm^3 (LICOR, 1992). The combined inlet tube and sample cell volume is 30.8 cm^3. The flow rate through the LICOR 6251 was not measured and this prevents direct calculation of the time lag. However, the phase difference between the w and CO_2 measurements can be estimated by finding the time lag that maximises the correlation between these two quantities. This analysis was done for

all grid flights and yielded a value of 1.0 ± 0.2 s for CO_2 while values for T_a and q were not significantly different from zero. CO_2 data from the LICOR 6251 have been advanced by 1.0 s prior to analysis to allow for the observed delay.

The flow rate through the LICOR 6251 can be estimated from the combined volume of the inlet tube and sample cell and the observed time lag between w and CO_2 by assuming that the lag equals the time for a parcel of air to be swept through the system. This gives an estimated flow rate of $1.8\ \mathrm{L\ min^{-1}}$. The speed of the air through the inlet tube and the sample cell can be calculated from the estimated flow rate and the cross-sectional area giving values of 2.5 and $0.4\ \mathrm{m\ s^{-1}}$ respectively. These values will be used when considering the attenuation of high frequency CO_2 concentration fluctuations.

The attenuation of high frequency fluctuations in trace gas concentration can be estimated from the physical dimensions of the tube and the speed of the flow (Leuning and King, 1992; Leuning and Judd, 1996). Attenuation is greater for laminar flow ($R_e < 2300$ where R_e is the Reynolds number) because of the deeper wall boundary layer and correspondingly larger radial diffusion in these conditions. Flow speeds in the inlet tube and the sample cell were 2.5 and $0.4\ \mathrm{m\ s^{-1}}$ respectively and the resulting Reynolds numbers for the inlet tube and the sample cell are 700 and 300 respectively so flow was laminar in both. Values for the coefficient in the transfer function describing the attenuation due to flow down the inlet tube and through the sample cell were calculated for the frequency range 0.01 to 10 Hz. These calculations showed that approximately 67% of the attenuation occurs in the sample cell and the remaining 33% in the inlet tube. However, the conditions inside the sample cell fall outside the range for which the method is valid (Leuning and Judd, 1996; Leuning and King, 1992) and the above percentages should be considered as first order approximations only.

Figure 3.12 shows plots of the spectra and cospectra with w of the CO_2 concentration measured by the LICOR 6251, specific humidity measured by the NOAA IRGA and specific humidity after applying the high frequency attenuation based on the theory in Leuning and Judd (1996). The data were collected during seven transect segments of 10 km in length and flown at an altitude of 26 m. The

attenuated specific humidity spectrum closely matches the observed CO_2 spectrum up to $n = 0.9$, after which the CO_2 spectrum departs from the expected form due to high noise levels. The attenuated cospectrum matches the observed CO_2 cospectrum up to $n = 0.3$ after which the CO_2 cospectrum drops more rapidly to zero than the filtered q cospectrum. The reason for this behaviour is examined in the next section. Although the theoretical expression provides a good fit to the observed spectrum, the faster decay of the cospectrum is better approximated by an enhanced triangle filter (Leise and Masters, 1991) with a cut-off frequency of 0.5 Hz, equivalent to $n = 0.33$ for the example in Figure 3.12. The final correction method adopted was to multiply the observed CO_2 flux by the ratio $\overline{w'q'}/\overline{w'q'_f}$ where q'_f is the turbulent fluctuation of specific humidity low-pass filtered with a cut-off frequency of 0.5 Hz. The size of the resulting correction decreases with increasing height above ground level with values of 1.25, 1.09, 1.04 and 1.01 at 18, 49, 156 and 260 m respectively.

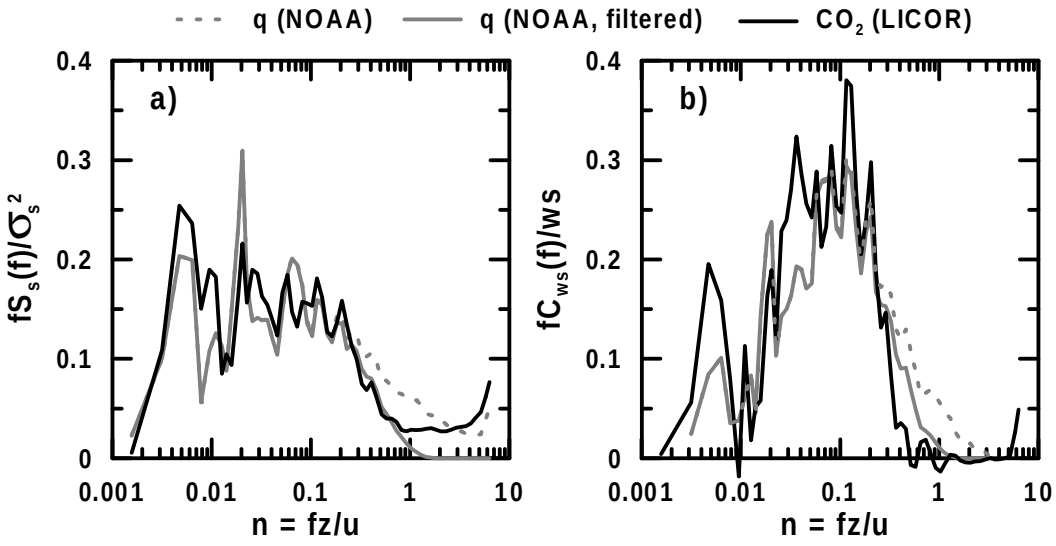

Figure 3.12 Plots of a) spectra and b) cospectra with w for specific humidity measured by the NOAA IRGA ("q (NOAA)", dashed grey), q filtered according to Leuning & Judd (1996) ("q (NOAA, filtered)", solid grey) and CO_2 measured by the LICOR 6251 ("CO_2 (LICOR)", solid black).

3.7.5 Phase Differences Between Scalars and w

The analysis of lagged correlation between various meteorological quantities measured on *HNK* did not reveal any phase differences except those associated with

flow through the inlet tube and sample cell of the LICOR 6251. However, lagged correlation is a gross measurement averaged over all frequencies and this may obscure frequency dependent phase differences that could lead to under-estimation of the turbulent fluxes. This section describes results from an analysis of phase spectra of data collected during the 1995 OASIS experiment.

Figure 3.13 shows plots of $w\theta$ and wq cospectra at 6, 20 and 50 m and phase spectra for $w\theta$ and θq at the same heights. At 6 and 20 m, the cospectra show a marked departure from the Kansas forms (Kaimal et al., 1972) at high frequencies for both $w\theta$ and wq. The cospectra at 50 m are much closer to the Kansas forms though still with a tendency to underestimate the covariance at higher frequencies.

The phase spectra are very similar at all heights. All show the phase difference between w and θ increasing at frequencies greater than about 1.5 Hz ($n \approx 0.3$ at 6 m, $n \approx 0.7$ at 20 m, $n \approx 2$ at 50 m). The same behaviour is observed between w and q (not shown) but the phase difference between θ and q remains small at all frequencies. No consistent phase difference was observed between w and u or v (data not shown).

The results show that there is a loss of correlation between w and the scalars θ and q at frequencies above about 1.5 Hz. This will lead to under-estimation of the turbulent fluxes when the aircraft height above ground level is less than 50 m, as was the case for most of the data collection flights during the 1995 OASIS experiment. A correction for the loss of covariance was estimated from the cospectral forms in Kaimal and Finnigan (1994) for the aircraft flights at 6, 20 and 50 m. These were 15, 10 and 2% respectively and the turbulent fluxes derived from the aircraft data have been corrected accordingly.

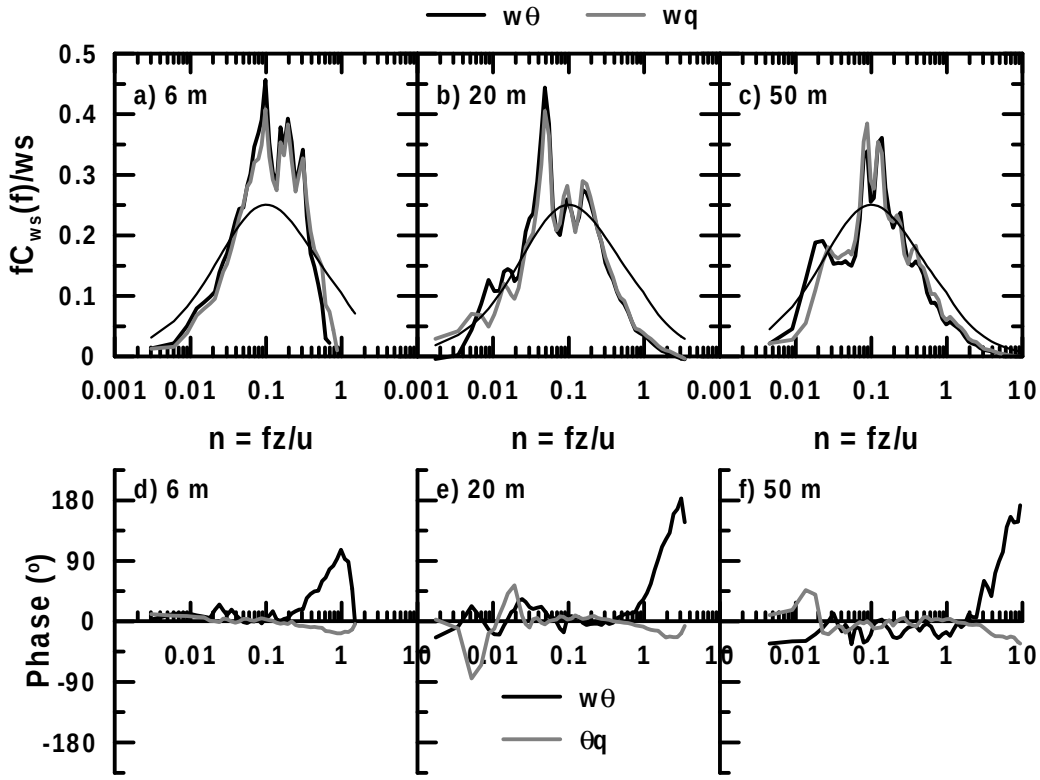

Figure 3.13 Plots of $w\theta$ and wq cospectra at a) 6 m, b) 20 m and c) 50 m and phase spectra of $w\theta$ and θq at d) 6 m, e) 20 m and f) 50 m. The Kansas cospectral forms (Kaimal and Finnigan, 1994) are plotted as thin black lines in a), b) and c).

3.8 Summary and Concluding Remarks

An extensive programme of calibrations was undertaken during the experimental work for this thesis. Such work had not formed part of the routine instrument maintenance at FIAMS due to operational constraints or had been performed but not documented. The aim of this chapter and the more detailed account in Isaac and Hacker (2004) is to fill this gap. The calibration techniques described in this chapter have not previously been applied to *HNK*. The motivations for this work were a belief that good measurements require well-calibrated instruments and that differences between sensors measuring the same quantity needed to be, and could be, resolved.

The PT100 fast response temperature sensors were calibrated in an ethanol bath at FIAMS and then adopted as the primary temperature sensor on *HNK* because of their simplicity and stability. The Meteolabor air and dew point temperature sensor was calibrated in an environmental chamber and the results agreed with the manufacturer calibrations. However, in-situ testing showed an offset of 2 - 3°°C in the thermocouple measurements of air and dew point temperatures from this instrument and this offset was traced to an incorrect measurement of the cold junction temperature. A laboratory calibration rig was established to enable the routine calibration of water vapour and CO_2 sensors. Repeated calibrations of the NOAA IRGA over several years showed that the H_2O and CO_2 sensitivities were stable to within 5%, adequate for measurement of the turbulent fluxes.

A calibration model for true airspeed proposed by Leise and Masters (1991) was adopted for use with *HNK*. The model assumes that the measured static pressure, dynamic pressure and air temperature are all subject to errors related to imperfect sensor design and flow distortion. It also provides a method of estimating the required empirical corrections using only the aircraft ground speed and radar altitude, thus avoiding the possibility of contamination from using the uncorrected pressures. Plausible values of the empirical correction parameters were obtained using data collected during a calibration flight in 1996 even though the flight took place in non-ideal conditions. The true airspeed calibration was further refined using data from

appropriate flights during the 1995 OASIS experiment. In particular, significant phase differences were found between the AHS-85 and GPS measurements of aircraft velocity and attitude.

Several problems with specific instruments were identified during the processing of data collected during the 1995 OASIS experiment. The most serious problems were the constriction of the pneumatic line to the total pressure sensor, the long response time of the reverse flow PT100 sensor and the attenuation of high frequency CO_2 concentration fluctuations in the air sampled by the LICOR 6251 analyser. Corrections for these problems have been developed and applied successfully to the data.

Much has been learnt about the instruments on *HNK* and this has resulted in increased confidence in the integrity of the data. However, there is room for improvement in some aspects of the aircraft instrumentation and operating practice in relation to the measurement of the turbulent fluxes in the boundary layer. First, a regular programme of instrument calibration and maintenance is required. This should include regular calibration flights to determine the empirical correction parameters and the flow angle calibrations. This is the only method by which the uncertainty in these numbers can be assessed. Second, fast response temperature and CO_2 sensors need to be investigated to improve the accuracy of sensible heat and CO_2 fluxes calculated from the aircraft data. Third, the thermal separation between the Meteolabor reference temperature and the actual cold junction of the air and chilled mirror thermocouples needs to be removed. This will remove the offset in the air and dew point temperatures from this instrument.